

The Formation of Stellar Clusters: Gaussian Cloud Conditions I

Ralf S. Klessen^{1,2} and Andreas Burkert¹

¹Max-Planck-Institut für Astronomie, Königstuhl 17, 69117 Heidelberg, Germany

²Sterrewacht Leiden, Postbus 9513, 2300-RA Leiden, The Netherlands

(accepted for publication in ApJSS)

ABSTRACT

The isothermal dynamical evolution of a clumpy molecular cloud region and its fragmentation into a protostellar cluster is investigated numerically. The initial density distributions are generated from different realizations of a Gaussian random field with power spectrum $P(k) \propto k^{-2}$. During the evolution of the system, the one-point probability distribution functions (pdf) of the gas density and of the line-of-sight velocity centroids develop considerable distortions away from the initial Gaussian behavior. The density pdf can be best described by power-law distributions, whereas the velocity pdf exhibits extended tails. As a result of the interplay between gas pressure and gravitational forces, a quasi-equilibrium clump mass spectrum emerges with a power-law distribution $dN/dM \propto M^{-1.5}$. Being part of a complex network of filaments, individual clumps are elongated, centrally condensed objects with 2:1 to 4:1 axis ratios with outer r^{-2} density distributions.

Dense, Jeans-unstable gas clumps collapse and form protostellar cores which evolve through competitive accretion and N -body interactions with other cores. In contrast to the clumps, the core mass spectrum is best described by a log-normal distribution which peaks approximately at the average Jeans mass of the system. Scaled to physical conditions typical for star-forming molecular clouds, the mass function is in good agreement with the IMF of multiple stellar systems.

The final dynamical state of the newly formed stellar cluster closely resembles observed young stellar clusters. It has a core/halo structure which is typical for collision dominated N -body systems. The 2-point correlation function of the spatial stellar distribution can be described by two power-laws with a break in the slope at the transition point from the binary to the large-scale clustering regime. The protostellar cluster is marginally bound and would be easily disrupted, if the conversion of cores into stars is inefficient.

Subject headings: hydrodynamics – ISM: clouds – ISM: kinematics and dynamics – ISM: structure – stars: formation – turbulence

1. Introduction

The formation of stellar clusters is yet an unsolved problem of theoretical astrophysics. Clusters form in giant molecular clouds complexes on time scales of order 10^6 yrs (Carpenter et al. 1997, Hillenbrand, 1997). This time scale is similar to the dynamical time scale of the clouds, it is however one order of magnitude shorter than the inferred cloud lifetime (Blitz & Shu 1980). The mechanisms that stabilize molecular clouds for such a long time are not well understood. Turbulence has been proposed to stir clouds, supporting them against gravitational collapse (Arons & Max 1975). Indeed, molecular emission lines tend to be an order of magnitude broader than the thermal linewidth (Blitz 1993), indicating supersonic velocities. Magnetic fields have been detected by direct measurements of field strength in some star forming regions (Myers & Goodman 1988, Crutcher et al. 1993 & 1999, Crutcher 1999, see however Verschuur 1995a,b) and may affect the cloud dynamics and stability.

Recent simulations suggest that freely decaying turbulence dissipates its kinetic energy on time scales shorter than a dynamical time scale (Gammie & Ostriker 1996, Mac Low et al. 1998, Stone, Ostriker & Gammie 1998), regardless of the adopted equation of state or the presence of magnetic fields. In order to stabilize clouds for a longer time, energy must be supplied, either by internal processes like stellar winds and outflows (Franco & Cox 1983, McKee 1989) or externally, e.g. by the shear motions induced through Galactic differential rotation (Fleck 1981). The spread in stellar ages for a given cluster is however similar to the dissipation time scale indicating that clusters form in regions where turbulence could decay leading to gravitational collapse. How turbulence is driven and why at some point in the evolution of the cloud the driving mechanism fails remains an outstanding issue.

Previous numerical models of isolated gaseous spheres have shown that stellar clusters could form as a result of gravitational collapse and fragmentation (see e.g. Larson 1978, Keto, Lattanzio & Monaghan 1991). These models were however strongly constrained by numerical resolution. More recently, Whitworth et al (1995), Turner et al. (1995) and Bhattal et al. (1998) investigated in detail the fragmentation of shocked interfaces of colliding molecular clumps into small stellar systems. The effects of gas accretion on the evolution of a newly formed, young stellar clusters has been investigated by Bonnell et al. (1997). They found that gas accretion is highly non-uniform with a few stars accreting significantly more than the rest and concluded that competitive accretion processes play an important role in shaping the initial stellar mass function. Finally, the individual collapse of perturbed protostellar cores and their break-up into binaries and multiple systems has recently been studied with high resolution (see e.g. Burkert & Bodenheimer 1993, 1996; Burkert, Bate & Bodenheimer 1997; Boss 1997, Truelove et al. 1997, 1998, Bate 1998).

In this paper we extend previous studies of the collapse of isolated gas clumps to the

molecular cloud regime and study the formation of stellar clusters localized within globally stable molecular clouds. Our simulations combine self-consistently previous studies of the dynamics of turbulent molecular clouds with studies of their collapse and fragmentation stage till the formation of a stellar cluster including its competitive accretion phase. In a previous short Letter (Klessen et al. 1998) we discussed a high-resolution simulation which lead to a stellar cluster with a log-normal mass distribution in excellent agreement with observations of multiple stellar systems. The current paper will explore the formation and early evolution of a star cluster in greater detail, starting from different initial realizations of clumpy molecular clouds with initial power-spectrum $P(k) \propto k^{-2}$. Section 2 presents the numerical method. Model properties and initial conditions are presented in section 3. The global evolution of the models is discussed in section 4. Section 5 analyzes the dynamics and structure of the gas cloud and the properties the newly formed stellar system and compares it with observations. Our results are summarized in section 6.

2. The numerical model

2.1. SPH in combination with GRAPE

SPH (*smoothed particle hydrodynamics*) is a particle-based scheme to solve the equations of hydrodynamics. As the fluid is represented by an ensemble of particles, the technique can be regarded as an extension of the pure gravitational N -body system. Besides being characterized by its mass m_i , velocity \vec{v}_i and location \vec{r}_i , each particle i is associated with a density ρ_i , an internal energy ϵ_i (equivalent to a temperature T_i), and a pressure p_i . The time evolution of the fluid is represented by the dynamical evolution of the SPH particles. Their behavior is governed by the equation of motion supplemented by additional equations to modify the hydrodynamic properties. Thermodynamic observables are obtained by averaging over an appropriate subset of the SPH particles. Excellent overviews over the method, its numerical implementation, and some of its applications have been written by Benz (1990) and Monaghan (1992). We use SPH because it is intrinsically Lagrangian: As opposed to mesh-based methods, it does not require a fixed grid to represent fluid properties and calculate spatial derivatives (see e.g. Hockney & Eastwood 1988). The fluid particles are free to move and – in analogy – constitute their own grid. The method is therefore able to resolve very high density contrasts because the particle concentration increases where needed.

Our code is based on a version originally developed by Benz (1990). It uses a standard description of a von Neumann-type artificial viscosity (Monaghan & Gingold 1983) with adopted parameters $\alpha_v = 1$ and $\beta_v = 2$ for the linear and quadratic terms. The system is

integrated in time using a second-order Runge-Kutta-Fehlberg scheme, allowing individual time steps for each particle. In any self-gravitating fluid, regions with masses exceeding the Jeans limit become unstable and collapse. In the current code, once a highly-condensed object forms in the center of a collapsing gas clump and has passed a certain density threshold, the dense core is substituted by a ‘sink’ particle (Bate, Bonnell & Price 1995). This particle has a fixed accretion radius, which is of order of the Jeans length at the density at which the sink particle is created. It inherits the combined masses, linear and ‘spin’ angular momenta of the particles it replaces. It has the ability to accrete further SPH particles from its infalling gaseous surrounding. Again, the mass of the accreted particles, their linear and angular momenta will be added to the sink particle in order to guarantee mass and momentum conservation. The accreted particles are then removed from the calculation. By adequately replacing high-density cores by sinks and keeping track of their further evolution in a consistent way the code time stepping is prevented from becoming prohibitively small and we are able to follow the dynamical evolution of the system over many free-fall times. However, this procedure implies that information about the evolution of gas inside the sink particle is lost. In our case a sink particle corresponds to a gravitationally collapsing protostellar core. For a detailed description of the physical processes inside a protostellar core, a new simulation just concentrating on this single object would be required with the appropriate initial and boundary conditions taken from the larger-scale simulation (Burkert, Klessen & Bodenheimer 1998).

To achieve high computational speed, we use SPH in combination with the special-purpose hardware device GRAPE (Sugimoto et al. 1990, Ebisuzaki et al. 1993). This device calculates the forces and the potential in the gravitational N -body problem by direct summation on a specifically designed chip with very high efficiency. This allows calculations at supercomputer level on a normal workstation. Additionally, GRAPE returns the list of nearest neighbors for each particle. This feature makes it attractive for use in smoothed particle hydrodynamics (Umemura et al. 1993, Steinmetz 1996). For particles near the surface of the integration volume, ‘ghost’ particles are created to correctly extend the neighbor search beyond the borders of the computational volume; no forces are computed for these particles.

Since we wish to describe the dynamical evolution of a gravitationally unstable region in the interior of a considerably larger globally stable molecular cloud, we adopt periodic boundary conditions to prevent overall collapse. As GRAPE cannot treat periodic particle distributions directly due to its restricted force we have to introduce the Ewald (1921) method to prevent global collapse. The basic idea is to compute a periodic correction force for each particle on the host computer, applying a particle-mesh like scheme: We first compute the forces in the isolated system using direct summation on GRAPE, then we assign the particle distribution to a mesh and compute the periodic correction force for each grid

point, by convolution with the adequate Green’s function in Fourier space. Finally, we add this correction to each particle in the simulation. The corrective Green’s function can be constructed as the offset between the periodic solution (calculated via the Ewald approximation) and the isolated solution on the grid. This method has proven to be numerically stable and inexpensive in terms of the computational effort (Klessen 1997).

2.2. Some cautionary remarks on the limitations of SPH

To make full use of the Lagrangian nature and resolving power of SPH the smoothing volume over which hydrodynamic quantities are averaged in the code is freely adjustable in space and time such that the number of neighbors considered is always kept in the range 30 and 70, with the optimum value being 50. This sets a natural limit to the spatial resolution of the code. It is furthermore constrained by the Courant-Friedrichs-Lewy (1928) criterion. It demands that the minimum time stepping in the SPH code is always less than the time required for a sound wave to cross the minimum smoothing volume. In order to prevent the time stepping required to resolve very high density peaks to become prohibitively small, one has to introduce a minimum smoothing length which defines the smallest resolvable length scale. In our simulations of self-gravitating gas the spatial resolution is subject to an additional constraint. In order to correctly treat the dynamical evolution of high-density peaks, the mass contained within the smoothing volumes of two interacting particles must be less than the local Jeans mass. Otherwise, the stability of the clump against gravitational collapse depends on the detailed implementation of the gravitational force law and on the kernel function used for the simulation, rather than on physical processes. The minimum Jeans mass that is reached during the calculation must always be greater than approximately twice the mass of particles in the SPH kernels (Bate & Burkert 1997). If one bears this caveat in mind, the SPH method calculates the time evolution of gaseous systems very reliably and accurately. Additionally it offers spatial and dynamical flexibility that has yet to be achieved by grid-based methods.

3. The model

The numerical models discussed in this paper describe self-gravitating, isothermal gas. This is justified by the typical densities observed in molecular clouds and determines the equation of state as well as the physical processes considered in the model. The dynamical evolution of the gas is scale-free and depends only on the ratio of the internal to gravitational energy. We start with an initially clumpy cloud region with density fluctuations following

a Gaussian random distribution. The velocities are computed self-consistently from the Poisson equation. Assuming that stellar clusters form through the gravitational collapse of clumpy cloud regions that have lost their turbulent support, we study the detailed behavior of this process and the properties of the newly formed cluster.

3.1. Scaling properties of isothermal, self-gravitating gas

For isothermal gas, the energy density is a function of temperature only and the equation of state reduces to $p = c_s^2 \rho$, with c_s being the thermal sound speed. This approximation is valid for physical regimes where the cooling time scales are much less than the dynamical ones. In molecular clouds, this is the case for gas densities $1 \lesssim n(\text{H}_2) \lesssim 10^{10} \text{ cm}^{-3}$, where the gas is optically thin for the dominant cooling processes and energy is radiated away very efficiently (e.g. Tohline 1982). Average densities in star forming regions typical are in the range $10 \text{ cm}^{-3} < n(\text{H}_2) < 10^5 \text{ cm}^{-3}$ which is the density range of our models. Even when resolving a density contrast of 10^4 , the isothermal equation of state is appropriate throughout the entire simulation.

The self-gravitating, isothermal model studies the interplay between gravity and gas pressure, it is thus scale free. Besides the dependence on the initial density and velocity distribution, the dynamical evolution of the system depends only on one additional free parameter, the ratio between the internal energy ϵ_{int} and the potential energy ϵ_{pot} . This ratio can be interpreted as a dimensionless *temperature*,

$$\alpha \equiv \epsilon_{\text{int}} / |\epsilon_{\text{pot}}|. \quad (1)$$

Line widths in molecular clouds are super-thermal, implying the presence of supersonic turbulent motions (e.g. Blitz 1993). In case of isotropic turbulence, these non-thermal (turbulent) contributions can be accounted for by introducing an *effective* energy $\epsilon_{\text{int}} = \epsilon_{\text{therm}} + \epsilon_{\text{turb}} = \gamma \cdot (c_s^2 + \sigma_{\text{turb}}^2) / 2$ adding up the thermal and non-thermal contributions to the kinetic energy. This is equivalent to defining an *effective* temperature α_{eff} . The turbulent velocity dispersion is denoted by σ_{turb} and the factor γ depends on the degree of freedom. In case of anisotropic turbulent motions, the system has (locally) preferred axes and the concept of one single effective temperature is not valid.

3.2. Normalization and relation to observed star-forming regions

In analogy to the temperature, we adopt dimensionless and normalized units for all physical quantities. All masses are scaled relative to the total mass of the simulated molecular

cloud region, and the length scale is its size L . The numerically simulated area is then a cube $[-L, +L]^3 = [-1, +1]^3$ with periodic boundary conditions. The density of the homogeneous cube is $\rho = 1/8$. In order to trigger gravitational collapse and star formation we consider systems that are highly unstable against gravitational collapse and set $\alpha = 0.01$. The volume will then contain $N_J = 222$ Jeans masses. We assume the gravitational constant $G \equiv 1$ and the gas constant $\mathcal{R} = 1/\gamma$ with $\gamma = 3/2$ for an ideal gas having three degrees of freedom. In these units the sound speed is $c_s = (\mathcal{R}\alpha)^{1/2}$ and the Jeans mass follows as

$$M_J = 1.6 \cdot \rho^{-1/2} \alpha^{3/2} . \quad (2)$$

In order to scale to physical units let us consider a dark cloud like Taurus with $n(\text{H}_2) \approx 10^2 \text{ cm}^{-3}$ and $T \approx 10 \text{ K}$. Assuming a mean molecular weight of $\mu = 2.36$, the units of mass and length correspond to $M = 6\,300 M_\odot$ and $L = 5.2 \text{ pc}$, respectively. The time unit is equivalent to $t = 2.2 \times 10^6$ years and the average Jeans mass transforms to $M_J = 28 M_\odot$. Applied to a dense, massively star-forming cloud with $n(\text{H}_2) \approx 10^5 \text{ cm}^{-3}$ and $T \approx 10 \text{ K}$, similar to the BN region in Orion, the simulated cube translates into a mass of $M = 200 M_\odot$ and a size scale $L = 0.16 \text{ pc}$. The time unit now converts to $t = 7.0 \times 10^4$ years and the mean Jeans mass for the homogeneous distribution is $M_J = 0.9 M_\odot$.

Molecular clouds are stabilized against global collapse by the presence of supersonic turbulence as indicated by the large observed line width (e.g. Blitz 1993). However, molecular clouds do form stars. Star formation occurs in their interior in regions which *locally* lose turbulent support and which begin to contract to form stars or clusters of stars. The time scale for freely decaying turbulence is of the order of the free-fall time or shorter (e.g. Mac Low et al. 1998). As the processes that lead to the local loss of turbulent support are not well understood, we do not attempt to model that stages of the evolution and start our simulations when turbulence has already decayed. This is equivalent to the assumption of instantaneous loss of support. The sizes of local collapse regions are typically much smaller than the overall extent of the cloud. To a good approximation we therefore neglect the influence of cloud boundaries and place the considered volume inside an infinite cloud. Hence, to describe a gravitationally unstable volume inside an overall stable cloud of much larger extent we adopt periodic boundary conditions. This is a commonly used scheme when describing turbulent cloud dynamics (e.g. Mac Low et al. 1998, Stone et al. 1998, Klessen 2000).

With the adopted values of $\alpha = 0.01$ collapse progresses quite rapidly and the influence of the boundary conditions on the overall dynamics is weak. The situation changes when the scaling parameter α is increased. The total number of Jeans masses contained in the computed cube then decreases, which in our isothermal models is equivalent to ‘zooming’ in onto smaller spatial volumes. Hence, the adopted boundary conditions become more important and may begin to influence the collapse behavior of individual protostellar cores.

As cores are never isolated, but instead interact with each other or accrete gas from their environment, in the case of $\alpha \gtrsim 0.1$ boundaries allowing for mass inflow would become more appropriate. Indeed, this study may be used for finding the optimum boundary conditions for high-resolution simulations which focus on the evolution of individual protostellar cores. We defer a detail discussion of this issue to paper II where we address the influence of different initial and boundary conditions. Decreasing α on the other hand means increasing the corresponding physical extend of the computed volume. The simulation treats a larger fraction of molecular cloud material and results in a larger number of protostellar cores that form during the dynamical evolution and fragmentation of the gas. This, however, also increases the computational demands (if a fixed mass and spatial resolution for individual cores is retained). The adopted value $\alpha = 0.01$ in the present paper corresponds to the maximum number of Jeans masses which we can handle with sufficient numerical resolution.

3.3. Initial conditions – Gaussian random fields

The dynamical evolution of gas in a molecular cloud region depends on its initial density and velocity distribution. In a self-consistent model, both are related via Poisson’s and the hydrodynamic equations. We adopt random Gaussian fluctuations for the density as starting condition for the SPH simulations. We use this approach, because these distributions have well determined statistical properties and can easily be generated by the Zel’dovich approach (see appendix B). Furthermore, their properties resemble the end stages of decaying turbulence and are suited to mimic observed features of molecular clouds once advanced into the non-linear regime (see e.g. Stutzki & Güsten 1990, who deploy a Gaussian decomposition technique to describe the clumpy structure of molecular clouds).

Gaussian random fields $\rho(\vec{r})$ are completely characterized by their first two moments, the mean value $\rho_0 \equiv \langle \rho(\vec{r}) \rangle_{\vec{r}}$ and the 2-point correlation function $\xi(\vec{r}) \equiv \langle \rho(\vec{r}') \rho^*(\vec{r} + \vec{r}') \rangle_{\vec{r}'}$, which is equivalent to the power spectrum $P(\vec{k})$ in Fourier space. All higher moments can be expressed in terms of $\xi(\vec{r})$. For an isotropic fluctuation spectrum, $P(k) = P(|\vec{k}|)$, the 2-point correlation degrades to a function of the distance between two points, $\xi(r)$. By defining a normalization ρ_0 and the power spectrum $P(k)$ in Fourier space, all statistical properties of the field $\rho(\vec{r})$ are determined.

The function $P(k)$ identifies the contribution of waves with wave number k to the statistical fluctuation spectrum. In Gaussian random fields, the phases are arbitrarily chosen from a *uniform* distribution in the interval $[0, 2\pi[$, and the amplitudes for each mode k are randomly drawn from a *Gaussian* distribution with width $P(k)$ centered on zero. Since waves are generated from random processes, only the properties of an *ensemble* of fluctuation fields

are determined in a statistical sense. Individual realizations (from different sets of random numbers) may deviate considerably from this mean value, especially at small wave numbers k , i.e. at long wave lengths, where only a few modes (k_x, k_y, k_z) contribute to the wave number $k = |\vec{k}|$. This means that different density fields generated from the same power spectrum $P(k)$ may *look* quite differently, especially on large scales (see Fig. 1), despite having identical statistical properties. This variance effect can be reduced by considering and averaging over a large enough ensemble of realizations. We generate the initial density fluctuation fields by applying the Zel’dovich (1970) approach. The method and its applicability to gaseous systems is discussed in detail in the appendix B.

In the current paper, we concentrate our analysis on a simple power-law functional form for the fluctuation spectrum, $P(k) \propto k^\nu$, with $\nu = -2$. As ν is a negative number, most power is in large-scale modes. This choice gives a good representation of the observed patchiness and inhomogeneity of molecular clouds. The dependence of the dynamical evolution of the model cloud on variations of the initial density distribution with different exponents ν of the power law will be discussed in paper II.

3.4. Model realization

We present results from a detailed analysis of nine different initial realizations of $P(k) \propto k^{-2}$ and use different particle numbers to address the issue of numerical resolution: six models with 50000 SPH particles, two with 200000 and one with 500000 particles, respectively. All models are generated using the Zel’dovich (1970) approximation (see appendix B) and their properties are summarized in Tab. 1. The projection into the xy -plane of the initial particle distribution in each model at the start of the dynamical evolution with SPH is presented in Fig. 1.

All but one model assume a random uniform particle distribution before applying the Zel’dovich shift. Placing particles randomly into a given volume produces an overall distribution that is homogeneous on large scales, but is subject to statistical fluctuations on small scales which introduce white noise into the correlation function. The scale at which this effect becomes important is of the order of the mean inter-particle distance. These undesired small-scale fluctuations may influence the fragmentation behavior of the gas. However, with the adopted temperature, the mass of small-scale regions of enhanced density is much less than the local Jeans mass. Therefore, these fluctuations are quickly damped and dynamically unimportant. As alternative to the random distribution, in model \mathcal{F} particles are placed on a regular grid before applying the Zel’dovich approximation. This distribution is force-free and has exactly uniform density. On the other hand, the grid has preferred axes

which introduce anisotropies in the neighbor list of each particle. This fact may again influence the small-scale behavior. On larger scales, the system is increasingly isotropic and this effect becomes negligible. In the hydrodynamic evolution phase after the Zel’dovich shift traces of the grid are quickly erased. Comparing the dynamical evolution, the model with the particles placed on a grid is statistically indistinguishable from the models generated from a random distribution, which we use as standard.

As discussed in appendix B, the Zel’dovich shift interval δt determines the density contrast in the particle distribution. Typically, larger δt leads to higher initial peak densities. On the other hand, smaller δt implies that a larger fraction of the total time evolution of the gas has to be computed with the SPH method and pressure forces, which are not included in the Zel’dovich approximation, have more time to act on the gas. In general, δt should be chosen small enough so that the subsequent evolution is not dependent on the choice of δt . In our models this is indeed the case for $\delta t \lesssim 2.0$ as is shown in appendix B.2. To address this issue further and to examine how a variation of the Zel’dovich shift interval influences the properties of the protostellar cluster that forms during the dynamical evolution and collapse of the gas, three models are generated with smaller shift intervals δt : model \mathcal{E} with $\delta t = 1.0$, and model \mathcal{H} together with the high-resolution model \mathcal{I} having $\delta t = 1.5$. Within the statistical variance between different models the results are not dependent on the initial shift interval.

4. Global time evolution

Due to the small value of α the gravitational energy outweighs the internal energy by far and the system is highly unstable to gravitational collapse and fragmentation. As a result, typically about sixty collapsed cores form during the dynamical evolution. A complete time evolution is illustrated in Fig. 2. Representative for all nine models it shows snapshots of the model \mathcal{A} at twelve different stages of its dynamical evolution. Note that the cube has to be seen periodically replicated in all directions. With the start of the SPH simulation, pressure forces begin to act on the gas and smear out fluctuations which are below the local Jeans limit. On the other hand, large modes are unstable against gravitational collapse and start to contract. At $t \approx 0.4$ the first highly-condensed cores form in the centers of the most massive and densest Jeans-unstable gas clumps and are replaced by sink particles (see Sec. 2). Soon, clumps of smaller initial mass and density follow. The density threshold for the formation of sink particles is chosen to be $\rho_c = 5000$ and the diameter of the sink particles is $1/100$ of the linear size of the simulated cube. It is visible in Fig. 2 that the system evolves into a network of intersecting sheets and filaments. The gas density is highest along filaments

and at their intersections. These are the locations where dense cores form predominantly and soon a hierarchically-structured cluster of accreting protostellar cores, represented by sink particles is built up. Whereas the overall dynamical evolution of the system is initially dominated by hydrodynamic effects (all the mass is in the gas phase), the later evolution is increasingly determined by the gravitational N -body interaction between protostellar cores and between cores and their clumpy gaseous environment because more and more gas is accreted onto dense cores. The final result is a bound dense cluster of protostars. After a few cluster crossing times, core motions have been randomized by close encounters and the protostars have lost knowledge of their initial conditions.

At this stage it is necessary to draw attention to one caveat: The gas in the models is treated isothermal. This implies that there exists no feedback mechanism which may prevent the complete accretion of all the gas into cores and at late phases the global core-formation efficiency*, defined by the percentage of gas that is converted into dense cores, approaches unity. This appears unphysical and is not observed in star-forming regions. At some stage during the protostellar evolution phase, feedback processes from nascent stars inside protostellar cores or from already existing massive stars in their vicinity will become relevant and terminate the accretion and collapse phase. These effects cannot be treated in an isothermal model. However, the early (isothermal) phases of the collapse of molecular cloud regions and the formation of a stellar cluster are well described. The time at which these assumptions become less appropriate is difficult to estimate. We are therefore hesitant to interpret the models beyond the phase at which more than $\sim 60\%$ of the gas has been accreted onto protostellar cores.

In Fig. 3, four stages of the evolution of the high-resolution model \mathcal{I} are presented. Figure 3 plots the system initially, at time $t = 1.4$, when 10% of the gas is condensed into protostellar cores and $t=2.0$ and $t=2.8$ when 30% and 60% of the total mass has been accreted, respectively. Instead of placing individual SPH particles, Fig. 3 plots the distribution of the gas density. The density field is scaled logarithmically with darker areas denoting higher densities. Hence, dark dots identify the location of dense collapsed cores. When comparing the time scales for core formation and subsequent accretion with the previous model, the different Zel'dovich shift intervals have to be taken into account. In the high-resolution calculation \mathcal{I} it is chosen to be $\delta t = 1.5$ instead of $\delta t = 2.0$ for model \mathcal{A} . Furthermore, the adopted accretion radius of sink particles in the code was reduced by a factor of two, it is now $1/200$ of the linear size of the simulation box. This delays the formation and accretion

*We use the word core-formation efficiency to distinguish from the commonly quoted star-formation efficiency. We identify the sink particles with unresolved, collapsing protostellar cores. Stars and cores are connected via the ability and effectiveness of *individual* cores to form stars.

onto sink particles by $\Delta t \approx 0.3$. Altogether, the state of the system where the mass fraction accumulated in collapsed cores exceeds a certain percentage is reached somewhat later by $\Delta t \approx 0.8$ in simulation \mathcal{I} . Besides this delay, the dynamical evolution of both systems is very similar, leading to the formation of a cluster of protostellar cores which grow in mass by accretion from its surrounding gas reservoir. We conclude that our basic results are not resolution dependent.

5. Discussion

Supplementing the general outline of the dynamical evolution in the last section, we now present a detailed analysis of the large-scale collapse and fragmentation behavior of the system. First, we discuss the one-point probability density functions of the density and of the distribution of line-of-sight velocity centroids. Then we describe the clumping properties of the gas at various stages of its dynamical evolution, the kinematic and spatial properties of the protostellar cluster that forms as the system advances in time and the mass spectrum of protostellar cores. Furthermore, we discuss the boundedness of the cluster and the rotational properties of protostellar cores. Finally, we speculate about the implications of our results for understanding the initial stellar mass function (IMF) by comparing the numerically calculated core mass spectrum with the IMF for multiple stellar systems.

5.1. Evolution of the one-point probability density functions for density and line-of-sight velocity centroids

There has been a series of recent attempts to use one-point probability density functions (pdf) as statistical descriptors of properties of the interstellar medium, in particular as diagnostic to distinguish between different physical processes influencing its dynamics and time evolution. For a discussion of the one-point probability density function of the density field and its relevance for the star formation process see e.g. Scalo et al. (1998a) and references therein. Detailed analyses of the pdf of line centroid velocity fluctuations are presented by Lis et al. (1996, 1998), Miesch, Scalo & Bally (1998), and Klessen (2000). Here we derive both sets of functions for our model of larger-scale cloud collapse.

5.1.1. The density pdf

We define the pdf of gas densities, $f(\rho)$, such that $f(\rho)d\rho$ measures the fraction of the total mass in the system that falls into the density range $[\rho, \rho + d\rho]$. The function $f(\rho)$ has of inverse density. Basically it is the histogram of the density summed over all SPH particles in the simulation. This defines $f(\rho)$ as *mass* weighted average. Note that some authors define the function by measuring the fractional *volume* occupied by gas within the density range $[\rho, \rho + d\rho]$. The later definition is convenient when analyzing numerical simulations performed with a grid-based method. SPH on the other hand is a particle based method, therefore it is more appropriate to obtain statistical measures by summing over the contributions of individual particles and hence obtain mass weighted averages.

Pure hydrodynamic simulations of turbulent isothermal gas *without* self-gravity or additional physical processes result in density pdf's of log-normal functional shape, i.e. the logarithm of the density follows a normal (Gaussian) distribution. However, there is increasing evidence that the inclusion of additional physical effects (like self-gravity or turbulent driving mechanisms) will lead to density pdf's which significantly deviate from being log-normal (Scalo et al. 1998, Passot & Vázquez-Semadeni 1998, Nordlund & Padoan 1998, Klessen 2000, Mac Low & Ossenkopf 2000).

This is also found in our simulations. Using data from the high-resolution simulation \mathcal{I} , Fig. 4 clearly shows that the evolution of Jeans unstable isothermal self-gravitating gas leads to *non*-log-normal density pdf's which can be described as power laws during most evolutionary stages. The initial state of the SPH evolution ($t = 0$, Fig. 4a) still exhibits a well established log-normal density pdf. This is expected after applying the Zel'dovich shift to transfer a Gaussian fluctuation spectrum – which has *per definitionem* a normal pdf in the linear regime – into the non-linear regime (Kofman et al. 1994). Later on self-gravity and gas pressure begin to shape the mass distribution into a network of intersecting sheets and filaments and ultimately into a cluster of collapsed dense cores (see Fig. 2 and 3). More and more gas converges into regions of high density and consequently the density pdf develops a high-density ‘tail’ of a power-law functional form. The power-law distribution is best established at that stage of the evolution, when the first and most massive Jeans unstable gas clumps have collapsed to high enough central densities that their innermost regions can be identified as compact cores (and subsequently are substituted by sink particles in our code). This happens at $t \approx 1.2$ and leads to a slope of the distribution function of $d \log_{10} N / d \log_{10} \rho = -0.8$ as can be seen in Fig. 4b. Densities of $\log_{10} \rho \approx 4$ in this figure arise from the contributions of the collapsed cores. For those, the values of $\log_{10} \rho$ are lower limits since they are computed by dividing the masses of the cores by their (fixed) volume; isothermal gas would continue to collapse to ever increasing central densities (until the gas

becomes optically thick and begins to heat up). Subsequently, with the number and masses of collapsed cores increasing, the density distribution is best described by multiple power laws. A steep part describes collapsing gas that forms a new core or that is accreted onto dense cores, and a shallower part that describes matter that does not (yet) participate in collapse and fills the low-density regions between filaments and cores (see Fig.’s 4c – e). In the final stage of the evolution (Fig. 4f) almost all of the mass is contained in a cluster of dense protostellar cores (with densities of $\log_{10} \rho \approx 4$) immersed into gas of low density exhibiting an almost flat density pdf.

In general, the spread and shape of pdf’s can be characterized by using their statistical moments. For each of the six epochs of simulation \mathcal{I} that are shown in Fig. 4 we compute the first four moments which are defined in the following way:

$$\text{mean} = \mu = \frac{1}{N} \sum_{i=1}^N \rho_i, \quad (3)$$

$$\text{standard deviation} = \sigma = \sqrt{\frac{1}{N} \sum_{i=1}^N (\rho_i - \mu)^2}, \quad (4)$$

$$\text{skewness} = \theta = \frac{1}{N} \sum_{i=1}^N \frac{(\rho_i - \mu)^3}{\sigma^3}, \quad (5)$$

$$\text{kurtosis} = \kappa = \frac{1}{N} \sum_{i=1}^N \frac{(\rho_i - \mu)^4}{\sigma^4}. \quad (6)$$

The summations extend over all $N = 500\,000$ SPH particles in the system. Mean μ and standard deviation σ quantify the location and the width of the pdf and are given in density units. The third and fourth moments are dimensionless quantities characterizing the shape of the distribution. The skewness θ describes the degree of asymmetry of the distribution around its mean. A negative value indicates an asymmetric tail extending towards the negative side, a positive value indicates a positive tail in the distribution. The kurtosis κ measures the relative peakedness or flatness of the distribution. Gaussian distributions are characterized by $\kappa = 3$. Smaller values indicate distributions that have flatter peaks, and larger ones point towards strong peaks or equivalently the existence of prominent tails. A pure exponential distribution leads to $\kappa = 6$. The values for model \mathcal{I} are listed in Tab. 2. Since we analyze a mass weighted density distribution, the first moment μ is not identical to the global average density, $\rho = 1/8$. Most of the mass is in gas of larger densities. Using only the first two moments (i.e. a Gaussian fit) to reconstruct the logarithmic density pdf never leads to a good representation of the data except for the initial configuration (Fig. 4a).

In summary, the filamentary morphology of the gas distribution and the power-law appearance of the density pdf in our models is clearly a result of the presence of self-gravity

which leads to collapse and compression and thus to the occurrence of high density contrasts. The hydrodynamic evolution of isothermal gas naturally produces log-normal density pdf's (see also Passot & Vázquez-Semadeni 1998). The inclusion of self-gravity leads to deviations from this simple analytical form towards more complex pdf's which during most stages of the dynamical evolution of the system can be described by power laws at the large density part of the distribution.

5.1.2. *The line-of-sight velocity centroid pdf*

One way to infer the three-dimensional structure of molecular clouds from the observed column density distribution is to include the velocity information along the line-of-sight. Using velocity coherence as indication for spatial correlation one is able to deconvolve the cloud into smaller subunits, i. e. into clumps on different scales. This is commonly applied to a variety of molecular clouds (Loren 1989, Stutzki & Güsten 1990, Williams et al. 1994, Onishi et al. 1996, Kramer et al. 1998, Heithausen et al. 1998) and we will discuss the clump structure of our models in the next section. However, other combinations of spatial and velocity information are possible and useful as well. There are attempts to characterize the structure of molecular clouds (and the turbulent interstellar medium in general) by using the pdf's of molecular line centroid velocity fluctuations (Miesch & Scalo 1995, Lis et al. 1998, Miesch et al. 1998). The idea is to determine the centroids of molecular lines for a large number of different positions across the face of a molecular cloud and from that compute their distribution function in velocity space. Like in the case of the density pdf, by doing so direct spatial information is lost, but the velocity centroid pdf still contains statistical information about the cloud and may be used to differentiate between different theoretical models. For instance, it has been shown experimentally and in numerical simulations that the pdf of the velocity field for incompressible turbulence is very nearly Gaussian although non-zero skewness should exist to some degree (e.g. Vincent & Meneguzzi 1991, Cao et al. 1996, Vainshtein 1997, Lamballais et al. 1997). This situation changes in the regime of highly compressible supersonic turbulence, the velocity pdf can deviate quite significantly from the Gaussian form (Lis et al. 1998, Klessen 2000, Mac Low & Ossenkopf 2000). This behavior is also found in the simulations of clustered star formation discussed in this paper. Here it is due to the presence of self-gravity which introduces strong collapse motions into the velocity field.

Again using data from the high resolution model \mathcal{I} , Fig. 5 shows centroid pdf's for the line-of-sight velocities along the x -, y -, and z -axis at four different stages of the dynamical evolution of the system, (a) at $t = 1.2$ just when the first dense cores have formed and

contain roughly 1% of the total mass, (b) at $t = 2.0$ when altogether 33 cores have formed and accreted 30% of the total mass, (c) at $t = 2.8$ when 60% of the available gas mass has been accreted, and finally (d) at $t = 3.9$ when 90% of the mass is accounted for by a cluster of 56 cores. We divide the face of the simulation cube into 50^2 cells of size 0.04^2 . For each cell, we compute the line profile by binning the normal (line-of-sight) velocity components of all gas particles that are projected into that cell; the width of each velocity bin is $\Delta v = 0.05$ which is 60% of the sound speed $c_s = 0.08$. This procedure corresponds to the formation of optically thin lines in molecular clouds where all molecules within a certain column through the clouds contribute to the shape and intensity of the line. We obtain the centroid of each line and the desired pdf by plotting the histogram of all centroid velocities. To reduce the sampling uncertainties, we repeat the same procedure, but with the location of each cell shifted by half a cell size. Altogether 5000 lines contribute to the pdf, each line being determined by the velocities of on average 200 SPH particles. The left column depicts the pdf for the line-of-sight along the x -axis (i.e. for particle projections onto the yz -plane), and the middle and right column for the y - and z -component, respectively. Note that in the linear-log plots the Gaussian distribution has a parabolic shape. The small inlay in the upper left corner of each histogram gives the *overall* line profile resulting from observing the entire cube, i.e. including the line-of-sight velocities of *all* gas particles in the system. Analog to plotting the pdf, the horizontal axis of the inlay gives the velocity in linear scale (each tick mark denoting a velocity increment $\delta v = 1.0$) and the vertical axis the logarithm of the number of particles that contribute to a velocity bin (with the separation of each tick mark being $\log_{10} N = 1.0$).

Since the thermal sound speed is $c_s = 0.08$ all line widths and the widths of the centroid pdf's are highly supersonic. Furthermore, none of the pdf's resembles a Gaussian. For comparison we have plotted for each of the pdf's a Gaussian curve constructed from using the first two moments of the distribution presented in Tab. 2 (the dashed parabolas in each plot). This curve never fits any of the pdf's and is typically too small in width. The distributions show extended tails and can appear quite asymmetric as indicated by the large values for the third and fourth moments, also listed in Tab. 2. Furthermore the pdf's show considerable substructure, for instance notice the double peaked distribution in Fig. 5b (z -component) or Fig. 5c (y -component). This is a sign of the streaming motion of gas onto a local center of gravity along filaments which by chance are aligned with the line-of-sight. Some pdf's show nicely developed exponential tails, like Fig. 5c (z -component) or Fig. 5d (y -component). As collapse and star formation progresses in time the width of the pdf's grows. However, pdf's at equal times but obtained from different projection angles also exhibit considerable deviations from each other. Depending on whether one looks along a major axis of contraction or perpendicular to it the width of the pdf appears larger or smaller. In

addition, massive gas clumps moving through the cloud will lead to individual features in the velocity pdf. Altogether, the clumpy structure of molecular clouds causes considerable substructure in the observed velocity pdf, it will never appear as a smooth function.

One of the implications from our sample is that the velocity centroid pdf’s in star forming regions are expected to drastically deviate from the Gaussian shape predicted from hydrodynamic turbulence models. This is indeed observed (Lis et al. 1998, Miesch et al. 1998). In our models this is due to the presence of self-gravity inducing strong contracting motions and clumpiness. However, other effects may lead to quite similar distortions as well (see Klessen 2000 for more details).

5.2. Evolution of clumps and cores

5.2.1. Clump mass spectrum

The structure of molecular clouds is extremely complex and observations reveal a network of intersecting filaments and clumps on all scales (e.g. Bally et al. 1987, Falgarone et al. 1992, Wiseman & Ho 1996). Molecular clouds may be fractal and various studies of the mass spectrum $N(m)$ of molecular clouds and of the gas clumps inside of clouds indicate that their distribution may be approximated by a power law of the form $dN/dm \propto m^\alpha$ with exponent $\alpha \approx -1.5$ (see e.g. Loren 1989, Stutzki & Güsten 1990, Williams et al. 1994, Onishi et al. 1996, Kramer et al. 1998, Heithausen et al. 1998). This universal law is an important constraint and test for models of molecular cloud evolution. Numerical simulations *must* be able to reproduce this structural feature of observed clouds. Indeed, our isothermal gas models naturally lead to a power-law clump mass spectrum which is a result of the interaction between gravity and gas pressure.

Representative for the entire set of isothermal larger-scale collapse calculations, Fig. 6 shows the mass distribution of clumps and condensed cores at four different stages of the dynamical evolution of the high-resolution model \mathcal{I} , namely initially and when 10%, 30% and 60% of the available gas has been accreted onto protostellar cores. For each of these times the upper panels compare the mass distribution of detected gas clumps (thin line) with the observed clump mass distribution $dN/dm \propto m^{-1.5}$, which translates into a slope of -0.5 when using logarithmic mass bins (dashed line). To identify individual clumps, we have developed a clump-finding algorithm similar to that of Williams et al. (1994), but based on the framework of SPH. For details see appendix A. The thick line depicts the mass distribution of condensed protostellar cores that have formed within the more massive gas clumps (a detailed analysis of this process is given in Sec. 5.2.2). The lower panels show the

position of each gas clump in a mass–density diagram. Clumps without cores are shown as crosses. Clumps containing one single core are denoted by open circles, those with multiple cores by filled circles. Unresolved, very condensed cores are plotted as stars with the density of cores being defined as the core mass divided by the volume within the fixed accretion radius. Therefore, they all fall along a straight line with slope 1/3. The isothermal Jeans mass as function of density is indicated by the diagonal line which separates the diagram into two regions. Clumps that lie to the right exceed their Jeans mass and are due to collapse, whereas clumps to the left are stabilized by gas pressure. The vertical line indicates the SPH resolution limit (Sec. 2.2). Clumps to the right of this line are well resolved, objects to the left are ill-defined and may be spurious results of the clump find algorithm.

The clumping properties in all simulations, from model \mathcal{A} with 50 000 SPH particles to model \mathcal{I} with ten times more particles, are remarkably similar. This suggests that the dominant dynamical processes are well treated and resolved. In all simulations, the clump spectrum of the initial gas distribution *cannot* be described by a simple power-law, it reflects the structural properties of the Gaussian random field from which the initial conditions are generated. The initially linear growth of density perturbations is not able to generate a hierarchical structure on all scales. This requires considerable non-linear gravitational evolution to take place. In the subsequent self-consistent dynamical evolution, the clump distribution quickly achieves a universal mass distribution with a power-law slope which is in excellent agreement with the observed exponent $\alpha \approx -1.5$ (dashed line). The core distribution, on the other hand, deviates significantly from a power-law distribution for smaller masses. Note, that the relative underabundance of low-mass cores with respect to low-mass clumps is not a resolution effect (see the vertical thin lines). All cores are well resolved in our models. Considerable deviations from a simple power-law spectrum of clump masses occur again in the very late phases of the evolution when most of the material is accreted onto dense cores and the gas reservoir becomes significantly depleted. Then, huge voids of very low density open up and the entire system more strongly resembles a (proto)star cluster than a molecular cloud. Within these two extreme phases of the isothermal gas evolution, from the linear initial gas distribution to the final star cluster, the complex interplay between gravity and gas pressure naturally creates a hierarchical structure with a distribution of clumps that is best described by a simple power-law, in agreement with the observations. As a reminder, when scaled to low density molecular cloud regions with densities $n(\text{H}_2) \approx 10^2 \text{ cm}^{-3}$ (e.g. Taurus) the total mass, $M = 1$, of the system corresponds to $6300 M_\odot$. When considering high density regions with $n(\text{H}_2) \approx 10^5 \text{ cm}^{-3}$ where clusters of stars can form (e.g. the BNKL-region in Orion) then the physical mass of our simulation is $200 M_\odot$ (see Sec. 3.2).

The lower panels in Fig. 6 indicate that initially only very few high-mass clumps exist which exceed the local Jeans mass. These clumps collapse rapidly and form the first con-

densed cores in their central region (see also Sec. 5.3.1). During the subsequent evolution the number of Jeans-unstable clumps and subsequently of protostellar cores increases, populating a larger region to the right of the diagonal line. If clumps merge which already contain protostellar cores, the new more massive clump will contain multiple cores in its interior. Competitive accretion (Price & Podsiadlowski 1995; Bonnell et al. 1997) and the gravitational interaction between the cores has important consequences for the further evolution. It influences their gas accretion and thus the final mass spectrum (more details are discussed in Sec. 5.2.3). These often unpredictable, probabilistic processes, resulting from chaotic multiple N -body interactions of cores, are responsible for the difference in the distribution of clump masses and of core masses. Whereas gas clumps evolve according to the laws of hydrodynamics, cores behave like accreting and gravitationally interacting N -body system. As a result, the mass spectrum of protostellar cores is well approximated by a log-normal functional form whereas the clump spectrum shows a power-law distribution.

5.2.2. Formation and mass growth of cores

The location and the time at which protostellar cores form, is determined by the dynamical evolution of their gas cloud. Besides collapsing individually, clumps stream towards a common center of attraction, where they may merge with each other or undergo further fragmentation. As can be seen in Fig.’s 2 and 3, isothermal models evolve into a network of intersecting sheets and filaments. The gas density is highest along filaments and at their intersections. These are the locations where dense cores form predominantly. The time of their formation in the centers of unstable clumps depends strongly on the relation between the time scales for individual collapse and fragmentation and clump-clump merging. When clumps merge that already contain cores the dynamical interaction between the cores becomes important.

As illustration, we show in Fig. 7 the accretion history for a number of selected protostellar cores (a) from model \mathcal{A} and (b) from model \mathcal{I} . The objects are numbered chronologically according to their time of formation. Model \mathcal{A} forms altogether 60 cores and model \mathcal{I} 55. The figure shows the following trends:

(a) The cores which form first tend to have the largest final masses. They emerge from clumps that were present from the beginning with the largest masses and highest densities and which are identified with the most significant peaks in the fluctuation field. Jeans unstable clumps with these qualities have very short collapse time scales. Hence, these clumps quickly form a single cores which are likely to accrete a large fraction of the parental gas before the dynamical evolution of their environment changes the clump properties too

much, i.e. before the clumps get dispersed or merge with other clumps. If a clump which already contains a core merges with a non-collapsed gas clump, for example when streaming along a filament towards a common center of attraction, then also the new clump is likely to become completely accreted onto these cores. Since the first cores form in the highest-density regions more or less independent of each other, their mass growth rate is dominated by the matter originating from their vicinity.

(b) On the other hand, matter that contracts into dense cores at later times ($t \gtrsim 2$) has already undergone considerable dynamical evolution. Clumps that were initially not massive enough to collapse onto themselves merge until enough mass is accumulated for them to collapse and build up a new protostellar core. This needs time. For those cores that form predominantly in the late stages of the dynamical evolution the available gas reservoir is already considerably depleted. Therefore, their average mass is rather small. The final mass of the protostellar cores (i.e. at the time when 90% of the available gas mass has been accreted) for the standard model \mathcal{A} and the high-resolution model \mathcal{I} in order of their formation is plotted in Fig. 8.

Another aspect of the accretion process onto individual cores is illustrated in Fig. 9. For the first nine cores (Fig. 9a) and for the last nine cores (Fig. 9b) that form in the high-resolution model \mathcal{I} , it plots the average initial distances at $t = 0.0$ between the accreted SPH particles and the particle that gets converted into the sink particle during the course of the simulation. This shows the volume from which particles accrete onto protostellar cores. As indicated above, the cores in Fig. 9a accrete most particles and the bulk of their final mass from their vicinity, i.e. from a distances less than ~ 0.5 . With the total size of the simulated cube being 2^3 , this corresponds to roughly $1/64$ of the total volume. If the material would be randomly sampled from a homogeneous cube of size 2^3 , the average distance would be ~ 1.3 . On the other hand, the smaller cores in Fig. 9b consist of matter that originates from a larger volume, much closer to the value for random sampling. This indicates that these clumps accrete from matter that already has undergone considerable dynamical evolution and is well mixed.

Further information about the processes determining the formation of and accretion onto dense cores is given in Fig. 10. It plots the contributions from individual clumps to the final mass of selected cores. As a general trend, cores that form very early can accrete a large fraction of their parental and neighboring clumps before clump interaction and merging becomes important. On the other hand, matter that builds up protostellar cores at the late stages of the dynamical evolution has participated in large-scale motions and successive clump merging. It is well mixed and the initial clump assignment is no longer significant. Furthermore, the competitive accretion amongst groups of cores in the interior of multiple

merged clumps becomes more important with the progression of time. This phenomenon also contributes to the distribution of available gas onto a larger number of cores. Therefore, the fraction $\langle f_j \rangle$ of material of individual clumps that gets accreted onto the cores decreases with time.

5.2.3. *The Importance of dynamical interaction processes*

Besides the effects discussed in the previous section, the growth rate of protostellar masses is strongly affected by the dynamical interaction between the cores themselves. This phenomenon is closely related to the competitive accretion of multiple cores within one common gas envelope (Price & Podsiadlowski 1995, Bonnell et al. 1997) and becomes important when clumps merge that already contain dense cores. In the center of the larger merged clump protostellar cores interact gravitationally with each other. Like in dense stellar clusters, close encounters may lead to the formation of unstable triple or higher-order systems and alter the orbital parameters of cluster members. During the decay of unstable subsystems, protostellar cores can get accelerated to very high velocities and may leave the cluster. During this process, the less massive cores are more likely to become ejected. Protostellar cores that get expelled from their parental clump are suddenly bereft of the massive gas inflow from their collapsing surrounding. They effectively stop accreting and their final mass is determined. The dynamical interaction between cores is an important agent in shaping the mass distribution.

As an example, we discuss the history of protostellar cores in the standard model. From Fig. 7a it is evident that core #5 stops accreting at $t \approx 0.8$, long before the overall gas reservoir is depleted. The same applies to core #7 at $t \approx 0.9$. In both cases, the objects were involved in a 3-body encounter that resulted in the expulsion from their gas rich parental clumps. Fig. 11 depicts the trajectories of the cores #3, #5, #11, #31, and #46. At $t \approx 0.3$ core #3 forms within an overdense region and slightly later cores #5 and #11 form in its vicinity from other Jeans-unstable density fluctuations. Their parental gas clumps merge and the whole systems flows towards a local minimum of the gravitational potential. The three cores soon build an unstable triple system, continuing to accrete from the converging gas flow they are embedded in (the detailed trajectories are shown in Fig. 11b, note the larger scale). At $t \approx 0.8$, core #5 is expelled and the remaining two cores form a wide binary, which at $t \approx 1.6$ suddenly hardens due to the gravitational encounter with core #46 (see Fig. 11c). Also this hard binary is transient, the interaction with core #31 pumps energy into its orbit, and in the subsequent evolution, the orbital period increases further during the encounter with a dense gas filament whose tidal influence finally disrupts the binary at $t \approx 2.4$. At

that time, accretion stops.

As another example from the high-resolution simulation, Fig. 7b shows that at $t \approx 1.8$, core #19 stops accreting. It is thrown out of a dense clump at the intersection of two massive filaments by a triple interaction with cores #1 and #17. However, it remains bound to the gas clump which grows in mass due to continuous infall and falls back into the clump and resumes accreting at $t \approx 2.0$. Cores #9 and #41 are also expelled from their parental clumps but, unlike core #17, their accretion is terminated completely. These dynamical interactions between protostellar cores influence their mass distribution significantly. In reality, ejected protostars may travel quite far and could explain the extended distribution of weak-line T Tauri stars found via X-ray observations in the vicinities of star-forming molecular clouds (e.g. Neuhäuser et al. 1995, Sterzik et al. 1995, Krautter et al., 1997, Wichmann et al. 1997).

As in our numerical scheme cores (i.e. sink particles) only interact gravitationally with each other, possible hydrodynamic processes are suppressed. Dense cores that come close to each other exert mutual tidal torques, they may merge or on the contrary strip off matter and loose mass during this process. However, we estimate these effects to be small. Matter accreted onto core particles would continue to collapse inwards to form a young stellar object surrounded by a disk on a very short time scale. The boundary introduced by the sink particle is determined by the resolution limit of the code. Scaled to physical units the diameter of the core particle is roughly 600 AU in case of high densities of $n(\text{H}_2) \approx 10^5 \text{ cm}^{-3}$ (as in the Orion star forming region) and about 10000 AU in low density regions like Taurus (using $n(\text{H}_2) \approx 10^2 \text{ cm}^{-3}$ and $T \approx 10 \text{ K}$). Matter inside the core is always expected to be strongly concentrated in the protostar in the center. The necessary cross section for merging or significant tidal perturbation (e.g. Hall, Clarke & Pringle 1996) is therefore typically much smaller than the size of the sink particles. To estimate how possible core mergers could influence the conclusions derived in this paper we took the initial conditions of simulation \mathcal{A} and repeated the calculation allowing for core particles to join together. We studied three different cases. The most stringent one was that we merged sink particles if they overlap by at least 90%, then if they overlap by 10% or more, and finally if two sink particles just touch each other. The resulting shape and width of the final core mass distribution remained essentially unchanged in all three cases compared to simulation \mathcal{A} , only the number of cores decreased.

5.3. Properties of (individual) gravitationally unstable clumps

5.3.1. *Properties of individual clumps*

Whereas the previous section discussed global features of the clump and core distribution, this section investigates in detail the properties of individual clumps. This is important for studies of the collapse of single clumps and their fragmentation into binaries and multiple stellar systems (Burkert & Bodenheimer 1993, Burkert & Bodenheimer 1996, Boss 1997, Burkert et al. 1998a, Burkert et al. 1998b). The simulations presented here are no longer able to resolve the collapse and sub-fragmentation of individual protostellar cores once they have been substituted by sink particles. To study this subsequent evolution, a new simulation just concentrating on the collapse of one single core would be required. To connect the final stages of the larger-scale simulations discussed here and the initial conditions for detailed collapse calculations, knowledge about the properties of individual cores is necessary. Important parameters are their density structure and their rotational properties. We note, however, that gas clumps are never isolated. Interactions with the environment are very important for the mass spectrum, the spatial distribution and the geometrical shape of clumps and cores.

The clumps generally are highly distorted and triaxial. Depending on the projection angle, they often appear extremely elongated, being part of a filamentary structure which may appear as a chain of connecting, elongated individual clumps. More complicated irregular shapes are also common which result from recent clump mergers at the intersections of filaments. A selection of clump shapes is presented in Fig. 12 which plots the contour lines for eight high-density clumps in simulation \mathcal{I} at time $t = 1.2$ projected into the xy -, xz - and yz -plane. At this state of the dynamical evolution, four collapsed cores have formed which accreted 1% of the total gas mass. This time is most appropriate to determine clump properties, because the system has already undergone substantial evolution (the power-law clump spectrum is well established) but most of the gas has not yet been accreted onto protostellar cores. The clumps that already formed dense cores in their interior are plotted in the first part of the figure, the second part shows clumps whose central densities are not yet high enough to form a condensed core. The clumps are numbered according to their peak density, i.e. clump #1 has the highest central density. The (surface) density contours are spaced logarithmically with two contour levels spanning one decade, $\log_{10} \Delta\rho = 1/2$. The lowest contour is a factor of $10^{1/2}$ above the mean density $\langle\rho\rangle = 1/8$. The black dots indicate the positions of the dense protostellar cores. Note the similarity to the appearance of observed dense (pre-stellar) clumps (for instance Fig. 1 in Myers et al. 1991). It is clearly visible that the clumps are very elongated. The ratios between the semi-major and the semi-minor axis measured at the second contour level are typically between 2:1 and 4:1. However, there may be significant deviations from simple triaxial shapes, see e.g. clump #4 which is located at the intersection of two filaments. This clump is distorted by infalling material

along the filaments and appears ‘y’-shaped when projected into the xz -plane. As a general trend, high density contour levels typically are regular and smooth, because there the gas is mostly influenced by pressure and gravitational forces. On the other hand, the lowest level samples gas that is strongly influenced by environmental effects. Hence, it appears patchy and irregular. The location of the condensed core within a clump is not necessarily identical with the center-of-mass of the clump, especially in irregularly shaped clumps.

Typically, the overall density distribution of identified clumps in our simulations follows a power law and the density increases from the outer regions inwards to the central part as $\rho(r) \propto 1/r^2$. For clumps that contain collapsed cores, this distribution continues all the way to the central protostellar object. However, for clumps that have not yet formed a collapsed core in their center, the central density distribution flattens out. As an example, Fig. 13 plots the averaged radial (surface) density profile of the xz -projection of clump #4 and of clump #12. This is in accordance with analytical models of isothermal collapse (see Larson 1969, Penston 1969; and also Whitworth & Summers 1985) and with the observational data for dense cores in dark molecular clouds (see e.g. Myers et al. 1991, Ward-Thompson et al. 1994, Chini et al. 1997, Motte et al. 1998).

5.4. Properties of the evolving protostellar cluster

5.4.1. Binarity and clustering properties of protostellar cores

An important statistical quantity derived from observational data is the 2-point correlation function or equivalently the mean surface density of companion stars ξ as function of separation r . Larson (1995) found that in the Taurus star-forming region the mean surface density of companions follows a power law as function of separation with a break in the slope at the transition from the binary to the large-scale clustering regime. It occurs at separations for which the binary system blend into the background distribution of cluster stars. This analysis has also been applied to other star-forming regions (Simon 1997, Bate et al. 1998, Gladwin et al. 1988). Larson identified the transition separation with the typical Jeans length in the molecular cloud. For Taurus this may be true. In Orion this conclusion fails. In general, it can be shown that the transition separation depends on the volume density of stars, the extent of the star-forming regions along the line-of-sight, the volume-filling nature of the stellar distribution and on the details of the binary distribution (Bate et al. 1998). Additionally, the transition separation evolves in time due to dynamical interactions amongst the cluster members. Note that the 2-point correlation function is never unique. It cannot differentiate between hierarchical (fractal) and non-hierarchical structure, and different stellar distributions may lead to the same 2-point correlation function. Therefore, the additional

analysis of the spatial distribution by eye is essential for a meaningful interpretation of ξ . Alternatively, to obtain quantitative results, the calculation of higher-order correlation functions may be useful, which is common in studying the large-scale structure of the universe (Peebles 1993). However, for star-forming regions this has never gone beyond the second order terms. Hence, we restrict our current analysis to a discussion of the 2-point correlation function ξ of the spatial distribution of protostellar cores (sink particles).

Figure 14 plots the mean surface density of companions ξ as function of separation r for the protostellar cluster that forms in the standard model \mathcal{A} at four different times of its evolution. At each point in time, the left panel gives the spatial distribution of the protostellar cluster projected in the xy -, xz - and yz -plane. The resulting functions ξ for each projection are shown in the right panel. We use data from model \mathcal{A} because it is the model which we advanced furthest in time. However, the conclusions apply to all models discussed in this paper: The initial binary fraction is very large. Roughly 75% of the cores are part of a (bound) binary or higher-order system which dominate the function ξ at small separations r . At larger r the function ξ flattens out which reflects the fact that the binary systems are relatively homogeneously distributed throughout the entire volume (Fig. 14a). The value of the plateau of ξ indicates the projected density of this homogeneous distribution.

At the intersections of filaments clumps which already contain one or more cores merge, forming larger clumps which subsequently contain a cluster of cores. As a result of this process, in Fig. 14b one sees several small aggregates distributed throughout the simulated volume. Within these small dense clusters complex dynamical interaction between cores takes place (cf. with Sec. 5.2.3) leading to the destruction of soft (i.e. weakly bound) binaries. At the same time hard binaries become even harder (i.e. more strongly bound) and the function ξ extends to smaller spatial separations. However, due to this secular evolution the overall binary fraction decreases. During the progression of the evolution, the small protostellar aggregates follow the streaming motion of their surrounding gas envelopes and merge, thereby forming a single bound cluster (see Fig. 14c). The protostellar system has reached a state of minimum spatial extent. The overall size of the cluster is reflected by the steep decline of the function ξ at large separations.

At that stage about 90% of the available gas has been accreted and the subsequent evolution of the cluster is almost entirely determined by gravitational N -body interactions. The cluster re-expands and rapidly develops a core/halo structure which is typical for collision-dominated self-gravitating N -body systems (see e.g. Binney & Tremaine 1987). This process is expedited by the fact that cores which have been accelerated to high velocities by close encounters with hard binaries cannot leave the simulation box due to the periodic boundary conditions. Once those ‘bullets’ have trespassed the boundaries of the cube, they are rein-

serted at the opposite side with the same velocity and may again interact with other cluster members to transfer energy to more slowly moving cores. In reality they would be ejected from the cluster and leave the star-forming cloud. At these late stages of the evolution, a clear change in the slope of the function ξ can be seen at the break between the binary regime and the large-scale clustering (see Fig. 14d). The fraction of fast moving ejected cores has grown to roughly 50%. At the same time, the binary fraction has decreased to 15%.

Duquennoy & Mayor (1991) analyzed a sample of nearby G-dwarfs and found that the distribution of orbital periods of binary stars in their sample follows approximately a broad Gaussian with a peak at $\sim 10^{4.8}$ days which corresponds to a separation of ~ 32 AU (using Kepler’s third law and assuming the typical mass of a G-dwarf is $\sim 1 M_{\odot}$). From the broad distribution of orbital periods it follows immediately that the function ξ of mean surface density of binary companions decreases with separation as $1/r^2$.[†] The same behavior is found in our systems. Figure 15 illustrates the distribution of semi-major axes for the identified *bound* pairs of cores in simulation \mathcal{A} at selected times. For each core its closest neighbor is found and if the pair is bound (i.e. if the sum of relative kinetic and potential energy is negative) the kinematic data at the present time are used to calculate the orbital parameters. In case of isolated pairs this works well, however, most cores are part of higher-order systems. In this case the given value is only a rough estimate of the true orbital characteristics as in unstable and highly chaotic few-body system well defined orbital parameters do not exist. We find that the logarithmic distribution of binary separations is broad and relatively flat and correspondingly that the function ξ falls off as $1/r^2$ in the binary regime (Fig. 14 at small r). When compared with the observations it should be noted furthermore that the systems of protostellar cores in our simulations correspond to wide binaries. Close binary system would form from *sub*-fragmentation of individual protostellar cores (e.g. Burkert & Bodenheimer 1996). This is a process which we cannot treat in the present numerical scheme. However, as indicated in Fig. 17, also the angular momenta of individual protostellar cores in our models follow a relatively flat and broad logarithmic distribution spanning at least three orders of magnitude. If we assume that a rotating protostellar core typically breaks up into a binary system with similar angular momentum the period distribution of close binaries should also be broad, as observed. This result follows from the stochastic processes which determine the formation and evolution of protostellar cores. They influence the properties of binary systems and at the same time also affect the angular momentum distribution of individual

[†]A broad distribution of orbital periods (in $\log_{10} P$) is equivalent to a broad distribution of binary separations $\log_{10} r$. To the lowest order it can be approximated as being flat, i.e. $dN/d\log_{10} r = K$. Then, $dN = K/r dr$ is the number of binary companions with separations in the range r to $r + dr$ and the mean surface density of companions in the 2-dimensional projection follows as $\xi(r) = N^{-1}dN/(2\pi r dr) = N^{-1}K/(2\pi r^2) \propto 1/r^2$.

cores.

5.4.2. Rotational properties of protostellar cores

A very important parameter for core collapse and possible sub-fragmentation is their specific angular momentum. Conservation of angular momentum prevents material from the envelope of a star forming core to directly accrete onto the central protostar. Only the inner part is able to immediately fall onto the star, the bulk of the infalling envelope accumulates in a rotationally supported disk around the central object. Angular momentum is transferred outward on viscous time scales τ_{vis} , by this moving matter inwards towards the central star. Typically, τ_{vis} is by a factor of 10 – 100 larger than the rotational time scale which is comparable to the free-fall time scale τ_{ff} (see e.g. Pringle 1981).

These processes take place deep inside the protostellar cores, hence they cannot be resolved by our numerical scheme. However, we can keep track of the the total angular momentum accreted onto each condensed core in our simulation. Figure 16 plots the time evolution of the angular momentum vector \vec{L} of all protostellar cores in the high-resolution model \mathcal{I} . The left panel describes the evolution of each individual component of the vector. The right panel plots the distribution of L_x , L_y and L_z at the end of the simulation at $t = 3.9$. For comparison, we overlay the final distribution (at $t = 5.6$) of the angular momenta of the cores in the standard model \mathcal{A} with dashed lines. Both distributions are statistically indistinguishable. From the plots, we see that the evolution of the angular momentum of individual cores can be very complex and intimately reflects the rotational properties of the environment they are embedded in: the angular momentum of the protostellar core is determined by the angular momentum of the clump it forms in. Clumps that merge at the intersection of two filaments can accumulate considerable angular momentum which is transferred onto the core by accretion. The angular momentum vector of cores may even change its sign if material is accreted which rotates counterclockwise with respect to the core.

The distribution of the absolute values of angular momenta $|\vec{L}|$ of the protostellar cores in simulation \mathcal{I} is plotted in Fig. 17a. Values are shown for $t = 2.8$ (solid line), i.e. when 60% of the gas is converted into dense cores, and at the final stage, $t = 3.9$ (dashed line). As already indicated in Fig. 16, the angular momenta are very broadly distributed and peak at $\sim 10^{-5}$. Note again that all values are given in dimensionless units with length and mass scales set to one. Figure 17b plots the distribution of the specific angular momenta $|\vec{L}|/m$ of the cores, again at $t = 2.8$ (solid line) and at $t = 3.9$ (dashed line). The mass dependence of $|\vec{L}|/m$ is shown in Fig. 17c. There are no massive cores with low specific angular momentum.

However, there is no clear correlation between both quantities.

Using the scaling properties discussed in Sec. 3.2, the dimensionless $|\vec{L}|/m$ values can be converted into physical units. When we apply our model to the high-density regime (e.g. to the BN region in the Orion molecular cloud with $n(\text{H}_2) \approx 10^5 \text{ cm}^{-3}$) then $|\vec{L}|/m = 1$ corresponds to $10^{23} \text{ cm}^2 \text{ s}^{-1}$. In the case of low densities of $n(\text{H}_2) \approx 10^2 \text{ cm}^{-3}$ (the average value in Taurus) this converts into $3.7 \times 10^{24} \text{ cm}^2 \text{ s}^{-1}$. The specific angular momenta of protostellar cores in our simulations are therefore of the order of 10^{20} to $10^{21} \text{ cm}^2 \text{ s}^{-1}$ and agree remarkably well with the observed values for wide binaries and protostellar objects (e.g. Bodenheimer 1995).

When looking at the spatial distribution of the angular momentum vectors of protostellar cores, there is a correlation between the location and the orientation. As is visible in Fig. 18, the angular momentum vectors of cores that form in the same region tend to be aligned. These cores form from gas that has similar global flow patterns. In clumps which contain multiple cores as the result of merging, all cores accrete from a common environment with a certain well defined angular momentum vector. As a result, the rotational properties of these cores tend to be comparable. In some star-forming regions, molecular outflows from young stellar objects indeed appear to be correlated and aligned (e.g. in the northern part of the L1641 cloud, see Fig. 14 in the review article by Reipurth 1989). Assuming that protostellar outflows are associated with the rotational properties of the protostellar object they emerge from, this implies a correlation between the angular momenta of the protostellar cores similar to the one found in our numerical models. On the other hand, in other regions no correlation is found at all (see Eislöffel & Mundt 1997, Stanke, McCaughrean & Zinnecker 1998, Reipurth, Devine & Bally 1998 for recent surveys). Taking all together, the observational data are not conclusive.

5.4.3. *Boundedness of protostellar clusters*

In the simulations described in this paper, the dynamical evolution of the gas results in the formation of dense clusters of collapsing cores that form protostars (see Fig.’s 2 and 3, and the left panels of Fig. 14). These clusters are bound throughout their entire evolution. To specify this in more detail, Fig. 19a plots for the protostellar clusters forming in simulation \mathcal{A} (dashed lines) and \mathcal{I} (solid lines) the time evolution of the total kinetic energy subdivided into the contribution from the internal velocity dispersion (thick line) and from the center-of-mass motion (thin line). The kinetic energy is almost entirely dominated by the internal random motions of the cluster members. In Fig. 19b, the evolution of the potential energy is given. Only the gravitational interaction between cores themselves is taken into account. The

potential of the gas in which the cluster is embedded is excluded in order to estimate whether the cluster would dissolve in case of a sudden removal of the gas. The cluster in the high-resolution model \mathcal{I} (solid lines) is still contracting when the simulation stops at $t = 3.9$. The cluster in model \mathcal{A} is allowed to evolve further and develops the typical core/halo structure of collisional N -body systems. The global virial coefficient $\eta_{\text{vir}} \equiv 2E_{\text{int}}/|E_{\text{pot}}|$ is plotted in Fig. 19c. Once the clusters have formed they remain marginally bound, i.e. $\eta_{\text{vir}} \lesssim 1$, even if all gas is removed. These conclusions do not change when taking into account only the cores that lie within the half-mass radius of the clusters. The cumulative mass of the clusters is given in Fig. 19d. For $t \geq 2.0$ more than 50% of the total mass is condensed into protostellar cores (sink particles). It is, however, interesting that already much earlier, during the formation of the cluster η_{vir} becomes constant with $\eta_{\text{vir}} \approx 0.7$. Dense protostellar cores tend to form such that the increase in the absolute values of the potential energy of the stellar cluster neglecting the potential of the gas component is always more or less balanced by an increase of its kinetic energy, even at very early times when the gravitational potential is strongly dominated by the gas. The 3-dimensional velocity dispersion and the line-of-sight velocity dispersion of the two clusters as function of time is described in Fig. 20. Again the dashed line denotes model \mathcal{A} and the solid line model \mathcal{I} . The fact that in our models the line-of-sight measurements along the different axes are almost identical to each other demonstrates that the cluster is kinematically well mixed and isotropic. When scaled to low-density star-forming regions like Taurus, a dimensionless value of $\sigma = 1$ corresponds to 2.2 km s^{-1} . In the case of a high-density region, this corresponds to 3.0 km s^{-1} (see Sec. 3). The values calculated from our simulations when roughly 50% to 60% of the gas has been accumulated in cores ($t \approx 2$) are in agreement with the measurements in Taurus and in the Trapezium cluster in Orion which both have comparable velocity dispersions of $\sigma \approx 2.5 \text{ km s}^{-1}$ (for Taurus see Frink et al. 1997, and for Orion see Jones & Walker 1988). However, for very high core-formation efficiencies, when more than 60% of the gas has been converted into condensed cores, the derived velocity dispersions appear to be too high. In order to reproduce the observed velocity dispersions we predict core formation efficiencies of order 50% to 60%. This is reasonable as one would expect that energetic feedback processes between the newly formed stars and their gaseous environment disperse gas clouds before they have completely condensed into stars. Note that the total star formation efficiency in the considered molecular cloud region is the product of the core formation efficiency and the efficiency with which the material accumulated in dense cores accretes onto their central stellar objects. The latter one is expected to be close to unity (for detailed simulations see Wuchterl & Tscharnuter 2000; for observational evidence see Motte, André & Neri 1998)

5.5. Implication for the IMF

In this section, the time evolution and the properties of the mass distribution of protostellar cores in our simulations and their relation to the initial stellar mass function are discussed. As analyzed in the previous sections, protostellar cores form in the centers of Jeans-unstable massive gas clumps and grow in mass via competitive accretion. This process is strongly influenced by the presence of unpredictable dynamical events which determine the shape of the mass spectrum. In Fig. 6 the mass distribution of identified gas clumps and protostellar cores in the high-resolution model \mathcal{I} has been introduced at four different stages of the dynamical evolution of the system, i.e. initially and when 10%, 30% and 60% of the available gas has been converted into condensed cores. Whereas the mass spectrum of gas clumps is best described by a power-law function, the distribution of core masses follows a Gaussian. Again for the high-resolution model, Fig. 21 plots the mass distribution of protostellar cores at times when the cluster of cores has accreted a total mass fraction of (a) $M_* = 5\%$, (b) 15%, (c) 30%, (d) 45%, (e) 60%, and (f) 85%. Spanning two orders of magnitude, the mass distribution of protostellar cores is very broad and peaks approximately at the overall Jeans mass of the system, $\langle M_J \rangle = 1/222 = 10^{-2.3}$ (see Sec. 3). This is somewhat surprising, given the complexity of the overall dynamical evolution. The Jeans mass is a function of density and may vary strongly for different clumps. In a statistical sense, the system retains ‘knowledge’ of its (initial) average properties and the ‘typical’ core mass is closely related to the ‘typical’ Jeans mass. In the initial conditions the density contrast is limited. Hence, the gravitationally unstable clumps which in Fig. 6 are located to the right of the tilted line indicating the Jeans limit as function of density, all have densities comparable to the mean density of the system, i.e. their local Jeans mass is $\sim \langle M_J \rangle$. These clumps form the first generation of cores which will become very massive and populate the upper end of the mass spectrum. At later stages, initially smaller clumps have merged and grown dense enough to become Jeans unstable too. They begin to collapse and form cores preferably at the low-mass end of the spectrum. As long as there is enough gaseous material, the growth rate of already existing cores to larger masses and the formation rate of new low-mass cores are comparable and the mass distribution evolves symmetrically (Fig. 21a – e). However, at very late stages of the evolution, the distribution gets skewed towards higher masses which is an effect of the depletion of the gas reservoir. There is still mass available for accretion, but it is not sufficient to form new cores (see Fig. 21a – f). The fact that the total gas reservoir is limited not only modifies the shape of the distribution, it also influences its peak value. At early stages, the median core mass is slightly below the average Jeans mass, at late stages it lies above (see also Tab. 3). Competitive accretion and the dynamical interaction of protostellar cores as members of dense clusters (see Sec. 5.2.3) do not alter the shape of the mass distribution, but may widen it further.

Figure 22 presents the mass spectra of protostellar cores for *all* simulations discussed in this paper (see Tab. 1) at the time when we would expect gas to be heated and dispersed by newly formed stars (see section 6.4.3), that is when roughly 60% of the gas is accumulated in protostellar cores. The distributions are very similar and the variations in widths and centroid are small. Since the data sets of observed protostellar cores are not yet large and accurate enough to derive well established mass distributions[‡], we have to go one step further and compare the core mass spectrum with the initial mass function of stars (IMF). The present simulations cannot resolve the conversion of individual protostellar cores into stars. Since detailed collapse simulations show that perturbed cores tend to break up into multiple systems we can only make predictions about the system mass function. We adopt the IMF for multiple stellar systems (i.e. without corrections for binary stars and higher-order systems) from Kroupa et al. (1990) which we compare with our numerically obtained core mass distribution. For this comparison we need to know the efficiency of individual dense cores to form stars inside. As their mass loss due to radiation, winds and outflows is expected to be small, most of the material accumulated in dense cores will be accreted onto the central protostars (Wuchterl & Tscharnuter 2000). Hence, we take the efficiency to convert dense cores into stars to be of order unity. The overall star-formation efficiency then depends only on the rate at which molecular gas forms dense cores. In general, this rate evolves with time and is determined by the properties of the underlying turbulent velocity field. This is particularly important in the case of ‘isolated’ star formation (Klessen, Heitsch & Mac Low 2000). Here, we concentrate on the ‘clustered’ mode of star formation and investigate molecular cloud regions where turbulence has decayed completely. The overall efficiency may also be influenced by the presence of massive O and B stars in the vicinity or within of the considered molecular cloud region. Once formed, their radiation would ionize the molecular gas and could prevent subsequent core formation and growth. As this effect is not included in our present investigation, the overall core formation efficiency therefore in principle remains a free parameter.

To estimate the appropriate density scaling in our models necessary for the computed and the observed mass distributions to agree, we require that both distributions peak at the same mass. Recall that the simulated core mass distribution reaches its maximum roughly at the overall Jeans mass of the system. To allow for a statistically significant comparison with observational data, we merge together the mass distribution of all nine models with $\alpha = 0.01$ and $P(k) \propto 1/k^2$. The resulting combined mass spectrum is shown in Fig. 23 at three stages of the evolution, when the fraction of mass in protostellar cores is $M_* = 30\%$,

[‡]For ~ 60 pre-stellar cores (i.e. for self-gravitating gas clumps without central collapsed object) in the ρ -Ophiuchus cloud, a mass spectrum is presented by Motte et al. (1998). See their Fig. 5.

$M_* = 60\%$, and $M_* = 90\%$, respectively. The best-fitting Gaussian representation of each distribution is plotted using open circles. The location of the centers and the widths are specified in Tab. 3. The log-normal description of the observed IMF for multiple stellar systems (the MS model in Kroupa et al. 1990) is indicated by the dashed lines. We use the following functional form,

$$\xi(\log_{10} m) = \xi_0 \exp \left[-\frac{(\log_{10} m - \log_{10} \mu)^2}{2(\log_{10} \sigma)^2} \right], \quad (7)$$

where $N = \xi(\log_{10} m)d\log_{10} m$ is the number of objects per logarithmic mass interval. The quantities m , μ and σ are given in units of the solar mass, $\log_{10} \mu$ and $\log_{10} \sigma$ determine peak and width of the distribution, and ξ_0 is the normalization. With this functional form the observed IMF peaks at $\log_{10} \mu = -0.31$ and has a width of $\log_{10} \sigma = -0.38$. For the efficiency $M_* = 30\%$, the core mass distribution has its maximum slightly below the average Jeans mass, $m_{\text{peak}} = 0.86 \langle M_J \rangle$. For agreement with the IMF the system needs to be scaled such that the average Jeans mass is $\langle M_J \rangle = 0.58 M_\odot$. For a gas temperature $T = 10$ K, this corresponds to a mean density $n(\text{H}_2) = 2.3 \times 10^5 \text{ cm}^{-3}$. For $M_* = 60\%$ and $M_* = 90\%$, where $m_{\text{peak}} = 1.4 \langle M_J \rangle$ and $m_{\text{peak}} = 2.0 \langle M_J \rangle$, these values are $n(\text{H}_2) = 6.2 \times 10^5 \text{ cm}^{-3}$ and $n(\text{H}_2) = 1.3 \times 10^6 \text{ cm}^{-3}$, respectively (see Tab. 3). These densities agree well with those observed in cluster forming regions (see e.g. Motte et al. 1998 for the ρ -Ophiuchus cloud). Note, that the width of the core mass distribution is slightly larger than the one of the IMF of multiple stellar system by Kroupa et al. (1990), however, it is somewhat smaller compared to the original Miller & Scalo (1979) mass function (their model of constant birthrate over 12×10^9 years has $\log_{10} \sigma = -0.68$; see the dotted lines in Fig. 23). Given the uncertainties involved in the observational determination of the IMF (e.g. Scalo 1986, 1998a) the agreement is remarkable and the significance of these deviations is low.

Our dynamical model of clustered star formation predicts a universal initial mass function with a log-normal functional form similar to the observational data for multiple stellar systems. The overall nature of the star formation process can only be understood in the framework of a statistical theory, where a sequence of probabilistic events may naturally lead to a log-normal IMF (e.g. Zinnecker 1990, Larson 1992, 1995, Richtler 1994, Price & Podsiadlowski 1995, Murray & Lin 1996, Elmegreen 1997; also Adams & Fatuzzo 1996). Since the final mass distribution of protostellar cores in our self-gravitating, isothermal models is a consequence of the chaotic dynamical evolution during the accretion phase, our simulations support this hypothesis.

6. Summary

In this paper we numerically investigated the dynamical evolution and fragmentation of molecular clouds and discussed the interplay between gravity and gas pressure. We identified the processes that dominate the formation and evolution of (proto)stellar clusters and determine their properties. From the results we can conclude that even simple, isothermal models of self-gravitating clumpy clouds are able to explain many of the observed features of star-forming regions. This is rather surprising, given the fact that magnetic fields and energetic heating processes of newly formed stars could in principle be important, both of which have been neglected. At this point the reader should be cautioned again that our isothermal models do not include any feedback effects from the star formation process itself. At late stages of the evolution energy and momentum input from young stars is likely to modify the dynamical properties of the accreting gas and the simple isothermal approach which we follow here needs to be extended by more elaborate schemes.

Our simulations show that, in general, the formation of a cluster of condensed cores and protostars through gravitational collapse and fragmentation of a molecular cloud region is extremely complex. The dynamical evolution of molecular gas is determined by the interplay between self-gravity and gas pressure. This creates an intricate network of filaments, sheets and dense clumps. Some clumps will become gravitationally unstable and undergo rapid collapse. While contracting individually to form protostellar cores in their interior, gas clumps stream towards a common center of attraction: the dynamical evolution of molecular clouds involves processes acting simultaneously on different length scales and time scales. While following the large-scale flow pattern, gas clumps can undergo further fragmentation or merge at the intersections of filaments. At that stage, the central regions of some clumps will have already collapsed to sufficiently high densities to be identified as protostellar cores. These cores rapidly grow in mass via accretion from their parental gas envelope. When clumps merge, the newly formed clump may contain a multiple system of protostellar cores which subsequently compete with each other for accretion from the same limited and rapidly changing reservoir of contracting gas in which they are embedded. Since the cores are dragged along with the global gas flow, a dense cluster of accreting protostellar cores builds up quickly. Analog to dense stellar clusters, its dynamical evolution is subject to the complex gravitational interaction between the cluster members: close encounters occur frequently and will drastically alter the orbital parameters of cores. This leads to the formation of unstable triple or higher-order systems, and consequently a considerable fraction of protostellar cores becomes expelled from the cloud. These cores effectively stop accretion and their final mass is determined.

The presence of unpredictable dynamical events in the overall gas flow and the evolution

of the nascent protostellar cluster very efficiently erases the memory of the initial configuration. For this reason, we cannot predict the detailed evolution of individual objects just from the initial state of the system. Only the properties of an *ensemble* of protostellar cores, for example their kinematics and mass distribution, can be determined in a probabilistic sense. A comprehensive theory of star formation needs to be a *statistical theory*. Some first attempts to formulate a statistical model of the star-formation process appear very promising (e.g. Zinnecker 1990, Larson 1992, 1995, Richtler 1994, Price & Podsiadlowski 1995, Murray & Lin 1996, Adams & Fatuzzo 1996, Elmegreen 1997; for an overview see Scalo 1998b) and are supported by the results of our numerical study. Taken together, our simulations strongly suggest that *gravitational* processes and accretion dominate the early phases of star formation.

We extend the above overview by giving a detailed list of the features and results of our calculations derived from the comparison of our numerical models with specific observational properties of molecular clouds and young stellar clusters:

- **One-point probability distribution function of density and line-of-sight velocity centroids:** During the dynamical evolution of the system gravitational contraction on large scales and the collapse of individual gas clumps result in considerable distortions of the pdf's away from the initial Gaussian behavior. The pdf of the logarithm of the density is best described by a (multiple) power-law distribution and the pdf of the line-of-sight velocity centroids develop extended high-velocity wings. This also holds for the line profiles themselves (Sec. 5.1).
- **Clump mass spectrum:** During the early phases of star formation our simulations of self-gravitating isothermal gas are able to reproduce the observed power-law clump-mass spectrum of molecular clouds. This is due to the progression of non-linear gravitational attraction and the disintegration of small clumps by gas pressure. The observed spectrum is best fit at times between the formation of the first condensed objects up to the time when depletion of the gas reservoir becomes considerable. Neither the initial Gaussian fluctuation spectrum, nor the final stages of the evolution when most of the gas is condensed into protostellar cores, give a clump-mass distribution which is in agreement with the observations. This is discussed in Sec. 5.2.1.
- **The Shapes of Individual Clumps:** Dense Jeans-unstable gas clumps are the precursors of protostellar cores. As being part of a complex network of filaments, individual clumps are typically very elongated objects with ratios between semi-major and semi-minor axis of 2:1 to 4:1. However, in many cases (especially at the intersection of two filaments) they can be quite irregularly shaped. These features are in agreement with observed dense pre-stellar cores in dark clouds (Sec. 5.3.1).

- **Formation and Growth of Protostellar Cores:** The formation and growth of protostellar cores is subject to a progression of statistical events. However, we can identify the following trends in our models (Sec. 5.2.2): (a) The protostellar cores that form first are generally formed in the clumps with the highest initial densities, and tend to have the highest final masses. They accrete the bulk of their final mass from their close vicinity. (b) On the other hand, matter that forms cores at later times has already undergone considerable dynamical evolution; these cores form from gas that was initially in widely distributed low-density clumps. Along filaments, they stream towards a common center of gravity and may merge at the intersections. Once enough mass is accumulated, these clumps undergo rapid collapse and build up new protostellar cores. The cores which form a late stages tend to have very low final masses.
- **Competitive Accretion and the Importance of Dynamical Interaction:** Once a gas clump becomes Jeans unstable it collapses and forms a condensed core. This core grows in mass via accretion from the infalling envelope. Merging may lead to clumps that contain multiple cores. These compete with each other for the material of a common gas reservoir. The succession of clump mergers leads to the formation of an embedded, dense protostellar cluster, whose dynamical behavior is dominated by close encounters between cluster members. Competitive accretion and collisional dynamics determine the kinematical and spatial properties of the cluster and the mass distribution of protostellar cores (Sec.'s 5.2.2 & 5.2.3).
- **Rotational Properties of Protostellar Cores:** The rotation of a protostellar core is an important parameter for its collapse. It determines the properties and stability of accretion disks and their tendency for sub-fragmentation. Within the complex network of intersecting filaments, gas clumps gain angular momentum from tidal torque and shear. In the accretion process it is transferred onto the embedded cores. Since the angular momentum is gained from large-scale motion, the orientation of the spin vectors of individual protostellar cores is correlated with their location (Sec. 5.4.2). A similar correlation is often found in observed star-forming regions between the orientation of the molecular outflows from young stellar objects and their location. However, the observational data are not conclusive.
- **Clustering Properties of Protostellar Cores:** The time evolution of a highly Jeans-unstable region within a molecular cloud leads to the formation of a dense cluster of protostellar cores. The final dynamical state of the system closely resembles the properties of observed stellar clusters: it exhibits the typical core/halo structure of collision-dominated N -body systems, and when calculating its 2-point correlation function, or equivalently the mean surface density of companions as function of separation,

one can clearly distinguish between the binary regime and the large-scale clustering regime (Sec. 5.4.1).

- **Boundedness of Protostellar Clusters:** The clusters of protostellar cores in our simulations form as bound entities: the conversion of gas into condensed cores is such that the decrease of potential energy is always balanced by the increase of kinetic energy (Sec. 5.4.3). Whereas the protostellar cluster is bound, this may not be true for the resulting stellar cluster. Its kinematical properties depend strongly on the details of the conversion of individual cores into stars: on the speed and the overall efficiency of the process. However, this cannot be treated in our simulations and needs to be addressed in detailed calculations of individual core collapse.
- **Mass Spectrum of Protostellar Cores — The Star Formation Efficiency and Implications for the IMF:** The distribution of stellar masses is one of the most important properties of the star-formation process. Any comprehensive model of star formation must be able to derive this quantity or at least address this issue. In our isothermal models the masses of protostellar cores are the result of a sequence of unpredictable stochastic events. In a natural way this leads to a *log-normal* mass spectrum which peaks roughly at the *average Jeans mass* of the system (Sec. 5.5). Detailed collapse calculations show that perturbed rotating cores tend to break up into multiple stellar systems, which cannot be resolved in the larger-scale simulations presented here. Therefore, we compare the numerical mass function of protostellar cores with the IMF derived for multiple stellar systems. Our simulations require densities in the range $n(\text{H}_2) = 10^5 \text{ cm}^{-3}$ to 10^6 cm^{-3} for both distributions to agree.

We thank Pavel Kroupa for valuable discussions on the topic of binary stars and the IMF, Philippe André for helpful comments and remarks on the mass spectrum of prestellar condensations, and Matthew Bate for his help with the SPH-code. We thank the referee for many useful comments and for the prompt reply.

A. The Clump Finding Method

This appendix describes the method used to identify the clumping properties of the numerical calculations. It applies a scheme similar to the one introduced by Williams et al. (1994), but which is fully integrated into the SPH formalism.

In SPH, the densities ρ_i of individual particles i are obtained in a local averaging process over a list of neighbors within distances less than twice the smoothing length h_i (e.g. Benz

1990, Monaghan 1992). To identify clumps, the resulting 3-dimensional density field is subdivided into ten bins equally spaced in the logarithm of the density. Starting with the highest density level, the particles are sorted by decreasing density, i.e. the first particle in the list is the one with the highest density. Going through this list, for each particle i it is checked whether the particles in its neighbor list are already assigned to a clump. If this is not the case, then particle i is assigned to a new gas clump, together with all the particles in its neighbor list. All additional particles at that level which are connected to the particles of the new clump by means of overlapping smoothing volumes are identified and assigned to the same clump. The assigned particles are finally removed from the density list. On the other hand, if the neighbor list of the tested particle i contains contributions from already identified clumps the particle will be associated to the clump that contributes the largest fraction of particles in the neighbor list, only particle i will be removed from the sorted list. This scheme is repeated until all particles at that density level are assigned to clumps. The procedure is repeated at the next lower level and so on up to the lowest level. The method is illustrated in Fig. 24. In the end, all SPH particles in the system are assigned to individual clumps.

This scheme is free of assumptions about the geometrical shape of the clumps[§] which is of great advantage when dealing with highly irregular and filamentary structure as in our numerical simulations of gravitational fragmentation and collapse. Note that two clumps that may at a high level of density be well separated entities, may at lower levels have common contour lines. In our scheme, they are still separated even at these lower levels by introducing an artificial ‘interface’ between the two clouds. Individual particles are *always* assigned to the clump that contributes most neighbors. This sets a clear division line between two competing clumps and enables their separation. Besides this basic separation criterion, the method is free of independent parameters and uses only intrinsic properties of the SPH scheme.

B. The Zel’dovich approximation and its validity to gaseous systems

B.1. The Zel’dovich Approximation

In 1970, Zel’dovich proposed for cosmological simulations a method to extrapolate the linear theory into the non-linear regime. The dynamical evolution of an idealized self-

[§]An alternative approach to determine clump properties in (observed) molecular clouds was introduced by Stutzki & Güsten 1990. These authors explicitly assumed that the gas clumps have Gaussian density profiles. They decomposed their intensity maps into clumps with such a profile by minimizing the residual.

gravitating and pressureless continuous medium can be expressed in terms of a function $\vec{f}(\vec{r}_0, \delta t)$. Its value is the position \vec{r} of a fluid element after a time interval δt , whose original position was \vec{r}_0 , i.e. $\vec{r} = \vec{f}(\vec{r}_0, \delta t)$. If we denote the original density field as $\rho(\vec{r}_0)$ then the density field after δt is given by

$$\rho(\vec{r}, \delta t) = \frac{\rho(\vec{r}_0)}{|\det f_{i,j}(\vec{r}_0, \delta t)|}. \quad (\text{B1})$$

Here, $f_{i,j}$ denotes the partial derivative of the i -th component of \vec{f} in \vec{r}_j . The time evolution is given by Poisson's equation and to first approximation it follows

$$\vec{r}(\delta t) = \vec{f}(\vec{r}_0, \delta t) = \vec{r}_0 + \vec{v}(\vec{r}_0) \delta t, \quad (\text{B2})$$

with $\vec{\nabla}_{\vec{r}_0} \cdot \vec{v}(\vec{r}_0) \propto \rho(\vec{r}_0)$. This assumes that the velocity field is rotation-free, because then the existence of a potential $\phi(\vec{r}_0)$ with $\vec{v}(\vec{r}_0) \equiv \vec{\nabla}_{\vec{r}_0} \phi(\vec{r}_0)$ is guaranteed and is connected to the density field via $\Delta_{\vec{r}_0} \phi(\vec{r}_0) \propto \rho(\vec{r}_0)$.

Using this method for the extrapolation of initially small density fluctuations into the non-linear regime (i.e. into regions where the density contrast exceeds the value of one) has certain limitations. For example, if $|\det f_{i,j}|$ becomes very small or zero, pressure forces would become important, preventing infinite densities. Furthermore, if one follows trajectories along which $|\det f_{i,j}|$ vanishes, the density decreases again after the singularity and at the same time the solution is no longer unique. For practical purposes by appropriately choosing the shift time δt one can minimize these problems and the Zel'dovich (1970) approximation is valid. We will show that this also applies for gaseous systems. This procedure considerably speeds up the computation of the early evolutionary phase since the system is advanced in one single large step as opposed to solving the complete set of hydrodynamic equations and integrating over many small time intervals.

We use the following method to generate random Gaussian fields: After the desired power spectrum $P(k)$ is defined we generate a *hypothetical* density field from all contributing modes in Fourier space (according to Sec. 3.3). This field is transformed back into real space and Poisson's equation is solved in order to obtain the velocities which would generate the density field self-consistently. Starting from a homogeneous initial density distribution, this velocity field is used to advance the particles in the system in one single large time step. As illustration, Fig. 25 plots the 2-dimensional projection of the homogeneous starting condition (Fig. 25a) and of the system after the Zel'dovich shift has been applied for various shift intervals δt (Fig. 25b – h). Note that the method implicitly assumes periodic boundary conditions. Therefore, the images have to be seen periodically replicated in all directions.

B.2. Validity of the Zel’dovich Approach

To test the validity of the Zel’dovich approximation and its parameter dependence we compare systems which have been generated with different sets of shift intervals δt and slopes ν of the power spectrum. Furthermore, we compare the results with systems that have been advanced in time using the full SPH formalism.

If particles move along trajectories on which $|\det f_{i,j}|$ vanishes the result is no longer unique, i.e. different paths may lead to the same location. For converging flows, the density increases before reaching the singularity in $|\det f_{i,j}|$ and decreases afterwards. This is unphysical for collision dominated systems. Depending on the size and the strength of individual fluctuations, the time interval δt to reach this singular point may differ. Assuming comparable amplitudes, for small perturbations δt will be short and for large-scale modes δt will be longer. This has to be taken into account when determining the optimum choice of the shift interval. The effect of varying δt is addressed in Fig. 25 which shows a sequence of particle distributions generated by the Zel’dovich method from a power spectrum $P(k) \propto k^{-2}$ with $0 \leq \delta t \leq 30$. The homogeneous starting field is identical to a shift of $\delta t = 0$. Increasing δt , the density contrast starts to grow and the distribution becomes more structured. However, at $\delta t \approx 3$ small-scale fluctuations begin to disperse again and the density contrast starts to diminish. At $\delta t \approx 30$ the system appears homogeneous again. The same is true for different slopes ν of the power spectrum. Figure 25i illustrates the dependence of the average (open circles) and maximum (solid circles) particle density on the time shift δt . The dashed line denotes the density of the homogeneous cube as reference.

Figure 26 describes the influence of different shift intervals δt on (a) the 2-point correlation function $\xi(r)$ and on (b) the measured power spectrum $P(k)$. In analogy to the above, the correlation strength and length increase with shift interval δt for systems generated with $t \lesssim 3$ and decrease again for larger shifts. Similar conclusions apply to the power spectrum. For $\delta t \approx 2$ the initial slope of $\nu = -2$ is best reproduced. Shorter shifts δt do not establish the mode spectrum sufficiently, the spectrum is too flat. Longer intervals produce overshooting on small scales, i.e. perturbations with short wave lengths are smeared out, whereas large modes are still amplified. Therefore the spectrum gets steeper. For $\delta t > 10$, overshooting occurs for the largest modes as well and the entire power spectrum flattens again.

Finally, we compare systems which have been generated by the Zel’dovich method with systems that have been advanced in time solely with SPH. The Zel’dovich shift generates fluctuations on all scales, since only gravitational forces are considered. Large perturbations are Jeans unstable and start to collapse. Most small ones are Jeans stable and pressure forces smear them out in the subsequent evolution with the SPH method. However, also some low-mass fluctuations may have been generated with sufficiently high density to be

gravitationally unstable, since the Jeans mass is inversely proportional to the square root of the density. These clumps will collapse as well. Furthermore, while flowing towards a common center of gravity small clumps may merge to form more massive clumps, which again may exceed the Jeans limit. The probability for that to happen depends on the time scale for the collapse and dispersal of individual clumps relative to the time scale for clumps to merge or fragment. This can be determined only in a statistical sense.

If we advance the system from the homogeneous state with the full SPH formalism, we compute the self-consistent initial velocity field of the hypothetical fluctuation field. Pressure forces are included from the beginning and small perturbations have no possibility to grow unless their mass exceeds the Jeans limit of the homogeneous system, which is determined by the mean density. Therefore, only high mass clumps can form. This is different from the Zel’dovich case, where perturbations are created on all scales and also some low-mass clumps may have large enough densities such that their local Jeans mass is smaller than the clump mass. Therefore, slightly smaller and more fragments are expected in systems that have been generated using the Zel’dovich method. The detailed discrimination of two systems subtly depends on the desired inhomogeneity and density contrast in the system, i.e. on the choice of ν and δt . These small-scale differences decrease, the more homogeneous the distribution and the smaller the Zel’dovich shift. On large scales, the statistical properties are much less affected.

This is exemplified, using a distribution of 50 000 particles with a power spectrum $P(k) \propto k^{-2}$. Again the simulation cube contains roughly 222 Jeans masses. Figure 27 shows snapshots of the time evolution of the system initially generated applying a Zel’dovich shift with $\delta t = 2$ and subsequently advanced with SPH. On the other hand, Fig. 28 describes the evolution of the system that was evolved from the homogeneous state using SPH without applying the Zel’dovich method. The large-scale behavior of the two systems is very similar, however differences on small scales occur. The distribution initially evolved with the Zel’dovich approximation is patchier at comparable times. Note, that time is measured from the begin of the evolution with SPH. To compare both systems at equal times, the Zel’dovich shift interval $\delta t = 2$ has to be added in Fig. 27. However, with the progression of the SPH calculation the higher degree of irregularity is reduced. Small perturbations are smoothed by pressure.

In summary, the Zel’dovich approximation is very well suited to generate fluctuation fields with well defined statistical properties determined by the power spectrum $P(k)$. With the appropriate choice of the shift interval δt , every spectrum can be generated. When applying the Zel’dovich method to gaseous systems, one has to take the effect of neglecting pressure forces into account. On small scales, small deviations from the fully self-consistent time

evolution may occur. Our test calculations do however show that applying the Zel’dovich method is fully appropriate for the purpose of the current investigation.

REFERENCES

- Arons, M., Max, C.: 1975. *ApJ*, 196, L77
- Adams, F. C., Fatuzzo, M.: 1996. *ApJ*, 464, 256
- Bally, J., Langer, W. D., Stark, A. A., Wilson, R. W.: 1987. *ApJ*, 312, L45
- Bate, M. R.: 1998. *ApJ*, 508, L95
- Bate, M. R., Burkert, A.: 1997. *MNRAS*, 288, 1060
- Bate, M. R., Clarke, C. J., McCaughrean, M. J.: 1998. *MNRAS*, 297, 1163
- Benz, W.: 1990, in *The Numerical Modelling of Nonlinear Stellar Pulsations*, ed. J. R. Buchler, p. 269, Kluwer Academic Publishers, The Netherlands
- Bhattal, A. S., Francis, N., Watkins, S. J., Whitworth, A. P.: 1998. *MNRAS*, 297, 435
- Binney, J., Tremaine, S.: 1987. *Galactic Dynamics*, Princeton University Press, Princeton, NJ
- Blitz, L.: 1993. in *Protostars and Planets III*, eds. E. H. Levy & J. I. Lunine, p. 125, Tucson, University of Arizona Press
- Blitz, L., Shu, F. H.: 1980. *ApJ*, 238, 148
- Bodenheimer, P.: 1995, *ARA&A*, 33, 199
- Bonnell, I. A., Bate, M. R., Clarke, C. J., Pringle, J. E.: 1997. *MNRAS*, 285, 201
- Boss, A. P.: 1997. *ApJ*, 483, 309
- Burkert, A., Bodenheimer, P.: 1993. *MNRAS*, 264, 798
- Burkert, A., Bodenheimer, P.: 1996. *MNRAS*, 280, 1190
- Burkert, A., Klessen, R. S., Bodenheimer, P.: 1998a. in *The Orion Complex Revisited*, eds. M. McCaughrean & A. Burkert, ASP Conference Series, in press
- Burkert, A., Bate, M. R., Bodenheimer, P.: 1998b. *MNRAS*, 289, 497
- Carpenter, J. M., Meyer, M. R., Dougados, C., Strom, S. E., Hillenbrand, L. A.: 1997. *AJ*, 114, 198
- Cao, N., Chen, S., She, Z.-S.: 1996. *Phys. Rev. Lett.*, 76, 3711

- Chini, R., Reipurth, B., Ward-Thompson, D., Bally, J., Nyman, L.-A., Sievers, A., Billawala, Y.: 1997. *ApJ*, 474, L135
- Courant, R., Friedrichs, K., Lewy, H.: 1928. *Math. Ann.*, 100, 32.
- Crutcher, R. M.: 1999, *ApJ*, 520, 706
- Crutcher, R. M., Troland, T. H., Goodman, A. A., Heiles, C., Kazes, I., Myers, P. C.: 1993. *ApJ*, 407, 175
- Crutcher, R. M., Troland, T. H., Lazareff, B., Paubert, G., Kazès, I.: 1999. *ApJ*, 514, L121
- Duquennoy, A., Mayor, M.: 1991. *A&A*, 248, 485
- Ebisuzaki, T., Makino, J., Fukushige, T., Taiji, M., Sugimoto, D., Ito, T., Okumura, S. K.: 1993. *PASJ*, 45, 269
- Eislöffel, J., Mundt, R.: 1997, *AJ*, 114, 280
- Elmegreen, B. G.: 1997. *ApJ*, 486, 944
- Ewald, P.P.: 1921, *Ann. Physik*, 64, 253
- Falgarone, E., Puget, J. L., Perault, M.: 1992. *A&A*, 257, 715
- Fleck, R. C. 1981. *ApJ*, 246, L151
- Franco, J., Cox, D. P. 1983. *ApJ*, 273, 24
- Frink, S., Röser, S., Neuhäuser, R., Sterzik, M. F.: 1997. *A&A*, 325, 613
- Gammie, C. F., Ostriker, E. C.: 1996. *ApJ*, 466, 814
- Gladwin, P. P., Kitsionas, S., Boffin, H. M. J., Whitworth, A. P.: 1999. *MNRAS*, 302, 305
- Hall, S. M., Clarke, C. J., Pringle, J.E.: 1996. *MNRAS*, 278, 303
- Hillenbrand, L. A.: 1997. *AJ*, 113, 1733
- Jones, B., Walker, M.: 1988. *AJ*, 95, 1755
- Heithausen, A., Bensch, F., Stutzki, J., Falgarone, E., Panis, J. F.: 1998. *A&A*, 331, L65
- Keto, E. R., Lattanzio, J. D., Monaghan, J. J.: 1991. *ApJ*, 383, 639
- Klessen, R. S.: 1997, *MNRAS*, 292, 11

- Klessen, R. S.: 2000, ApJ, in press
- Klessen, R. S., Burkert, A., Bate, M. R.: 1998. ApJ, 501, L205
- Klessen, R. S., Heitsch, R., Mac Low, M.-M.: 2000, ApJ, in press
- Kofman, L., Bertschinger, E., Gelb, J. M., Nusser, A., Dekel, A.: 1994. ApJ, 420, 44
- Kramer, C., Stutzki, J., Rohrig, R., Corneliussen, U.: 1998. A&A, 329, 249
- Krautter, J., Wichmann, R., Schmitt, J. H. M. M., Alcalá, J. M., Neuhäuser, R., Terranegra, L.: 1997. A&A, 123, 329
- Kroupa, P., Tout, C. A., Gilmore, G.: 1990. MNRAS, 244, 76
- Kroupa, P., Tout, C. A., Gilmore, G.: 1993. MNRAS, 262, 545
- Lamballais, E., Lesieur, M., Métais, O. 1997, Phys. Rev. E, 56, 761
- Larson, R. B.: 1969. MNRAS, 145, 271
- Larson, R. B.: 1978. MNRAS, 184, 69
- Larson, R. B.: 1992. MNRAS, 256, 641
- Larson, R. B.: 1995. MNRAS, 272, 213
- Lis, D. C., Pety, J., Phillips, T. G., Falgarone, E. 1996, ApJ, 463, 623
- Lis, D. C., Keene, J., Phillips, T. G., Pety, J. 1998, ApJ, 504, 889
- Loren, R. B.: 1989. ApJ, 338, 902
- Mac Low, M.-M., Klessen, R. S., Burkert, A., Smith, M.D.: 1998. Phys. Rev. Lett., 80, 2754
- Mac Low, M.-M., Ossenkopf, V.: 2000. A&A, 353, 339
- McKee, C. F.: 1989. ApJ, 345, 782
- Miesch, M. S., Scalo, J. M.: 1995. ApJ, 450, L27
- Miesch, M. S., Scalo, J. M., Bally, J.: 1998. ApJ, submitted (astro-ph/9810427)
- Monaghan, J. J.: 1992. ARA&A, 30, 543
- Monaghan, J. J., Gingold, R. A.: 1983. Journ. Comp. Phys., 52, 135

- Motte, F., André, P., Neri, R.: 1998. *A&A*, 336, 150
- Murray, S. D., Lin, D. N. C.: 1996, *ApJ*, 467, 728
- Myers, P. C. , Goodman, A. A.: 1988 *ApJ*, 326, L27
- Myers, P. C., Fuller, G. A., Goodman, A. A., Benson, P. J.: 1991. *ApJ*, 376, 561
- Neuhäuser, R., Sterzik, M. F., Torres, G., Martin, E. L.: 1995. *A&A*, 299, L13
- Nordlund, Å, Padoan, P.: 1998, in *Interstellar Turbulence*, eds. J. Franco & A. Carraminana, Cambridge University Press, in press
- Onishi, T., Mizuno, A., Kawamura, A., Ogawa, H., Fukui, Y.: 1996. *ApJ*, 465, 815
- Passot, T., Vázquez-Semadeni, E. 1998, *Phys. Rev. E*, 58, 4501
- Peebles, P. J. E.: 1993. *Principles of Physical Cosmology*, Princeton University Press, Princeton, NJ
- Penston, M. V.: 1969. *MNRAS*, 144, 425
- Price, N. M., Podsiadlowski, P.: 1995. *MNRAS*, 273, 1041
- Pringle, J. E.: 1981. *ARA&A*, 19, 137
- Reipurth, B.: 1989. in *Low-Mass Star Formation and Pre-Main Sequence Objects*, ed. B. Reipurth, Vol. 33 of *ESO Conference Proceedings*, p. 247, Garching, Germany
- Reipurth, B., Devine, D., Bally, J.: 1998. *AJ*, 116, 1396
- Richtler, T.: 1994. *A&A*, 287, 517
- Salpeter, E. E.: 1955. *ApJ*, 121, 161
- Scalo, J.: 1986. *Fund. of Cosmic Physics*, 11, 1
- Scalo, J.: 1998. in *The Stellar Initial Mass Function*, eds. G. Gilmore, I. Parry & S. Ryan, *PASP Conf.* (astro-ph/9812327)
- Scalo, J.: 1998. in *The Birth of Galaxies*, Blois, France (astro-ph/9811341)
- Scalo, J., Vázquez-Semadeni, E., Chappell, D., Passot, T.: 1998, *ApJ*, 504, 835
- Simon, M.: 1997. *ApJ*, 482, L81

- Stanke, T., McCaughrean, M. J., Zinnecker, H.: 1998, *A&A*, 332, 307
- Sterzik, M. F., Alcalá, J. M., Neuhäuser, R., Schmitt, J. H. M. M.: 1995. *A&A*, 297, 418
- Steinmetz, M.: 1996. *MNRAS*, 278, 1005
- Stone, J. M., Ostriker, E. C., Gammie, C. F.: 1998. *ApJ*, 508, L99
- Stutzki, J. Güsten, R.: 1990. *ApJ*, 356, 513
- Sugimoto, D., Chikada, Y., Makino, J., Ito, T., Ebisuzaki, T., Umemura, M.: 1990. *Nature*, 345, 33
- Tohline, J. E.: 1982. *Fund. of Cosmic Physics*, 8, 1
- Turner, J.A., Chapman, S.J., Bhattal, A.S., Disney, M.J., Pongracic, H., Whitworth, A.P.: 1995. *MNRAS*, 277, 705
- Truelove, J. K., Klein, R. I., McKee, C. F., Holliman, J. H., Howell, L. H., Greenough, J. A.: 1997. *ApJ*, 489, L179
- Truelove, J. K., Klein, R. I., McKee, C. F., Holliman, J. H., Howell, L. H., Greenough, J. A., Woods, D. T.: 1998. *ApJ*, 495, 821
- Umemura, M., Fukushige, T., Makino, J., Ebisuzaki, T., Sugimoto, D., Turner, E. L., Loeb, A.: 1993. *PASJ*, 45, 311
- Vainshtein, S. I. 1997, *Phys. Rev. E*, 56, 6787
- Vázquez-Semadeni, E.: 1994. *ApJ*, 423, 681
- Verschuur, G.L.: 1995a. *ApJ*, 451, 624
- Verschuur, G.L.: 1995b. *ApJ*, 451, 645
- Vincent, A., Meneguzzi, M.: 1991. *J. Fluid Mech.*, 225, 1
- Ward-Thompson, D., Scott, P. F., Hills, R. E., Andre, P.: 1994. *MNRAS*, 268, 276
- Whitworth, A., Summers, D.: 1985. *MNRAS*, 214, 1
- Whitworth, A. P., Chapman, S. J., Bhattal, A. S., Disney, M. J., Pongracic, H., Turner, J. A.: 1995. *MNRAS*, 277, 727.
- Wichmann, R., Krautter, J., Covino, E., Alcalá, J. M., Neuhäuser, R., Schmitt, J. H. M. M.: 1997. *A&A*, 320, 185

Williams, J. P., De Geus, E. J., Blitz, L.: 1994. *ApJ*, 428, 693

Wiseman, J. J., Ho, P. T. P.: 1996. *Nature*, 382, 139

Wuchterl, G., Tscharnuter, W. M.: 2000. *A&A*, submitted

Zel'dovich, Y. B.: 1970. *A&A*, 5, 84

Zinnecker, H.: 1984. *MNRAS*, 210, 43

Zinnecker, H.: 1990. in *Physical Processes in Fragmentation and Star Formation*, eds. R. Capuzzo-Dolcetta & C. Chiosi, p. 201, Kluwer Academic Publishers, The Netherlands

Tables:

Table 1: Summary of the numerical models, all with temperature $\alpha = 0.01$ and power spectrum $P(k) \propto 1/k^2$.

Model	Particle Number	Initial Distribution ^a	Zel'dovich Shift ^b
\mathcal{A}	50 000	random	$\delta t = 2.0$
\mathcal{B}	50 000	random	$\delta t = 2.0$
\mathcal{C}	50 000	random	$\delta t = 2.0$
\mathcal{D}	50 000	random	$\delta t = 2.0$
\mathcal{E}	50 000	random	$\delta t = 1.0$
\mathcal{F}	50 000	grid	$\delta t = 2.0$
\mathcal{G}	200 000	random	$\delta t = 2.0$
\mathcal{H}	200 000	random	$\delta t = 1.5$
\mathcal{I}	500 000	random	$\delta t = 1.5$

^aInitial distribution for the Zel'dovich shift. A homogeneous random distribution is denoted by ‘random’, whereas ‘grid’ means that the particles have initially been placed on a regular grid.

^bShift interval δt for the Zel'dovich approach.

Table 2: Moments of the density and of the line-of-sight velocity centroid pdf

	x	y	z	$\log_{10} \rho$
$t = 0.0$ — no cores have formed yet				
μ	-0.03	-0.02	-0.02	-0.69
σ	0.02	0.03	0.02	0.38
θ	0.06	-0.04	-0.09	0.22
κ	1.00	1.00	1.01	2.91
$t = 1.2$ — 6 cores with $M_* = 1\%$				
μ	-0.03	-0.02	-0.01	-0.68
σ	0.04	0.07	0.12	0.51
θ	-0.34	-0.16	-0.34	1.52
κ	5.11	4.30	2.19	7.19
$t = 1.5$ — 15 cores with $M_* = 10\%$				
μ	-0.03	-0.01	-0.01	-0.56
σ	0.07	0.13	0.21	0.78
θ	-0.20	-0.49	-0.07	1.47
κ	6.59	3.53	1.95	5.30
$t = 2.0$ — 31 cores with $M_* = 30\%$				
μ	-0.04	0.00	-0.07	-0.42
σ	0.11	0.20	0.30	0.98
θ	0.91	-0.34	0.20	0.84
κ	7.31	4.48	2.64	3.04
$t = 2.8$ — 51 cores with $M_* = 60\%$				
μ	-0.07	0.03	-0.06	-0.28
σ	0.19	0.36	0.37	1.14
θ	0.55	-0.15	0.03	0.28
κ	6.31	4.83	4.92	2.61
$t = 3.9$ — 56 cores with $M_* = 90\%$				
μ	0.00	0.08	-0.06	-0.44
σ	0.32	0.36	0.34	1.17
θ	-0.70	0.77	1.61	0.42
κ	8.59	7.55	11.73	3.47

The first four moments μ , σ , θ , and κ , respectively, as defined in Eqn.’s 3 to 6, of the distribution of the line-of-sight velocity centroids (x -, y -, and z -component) and of the logarithm of the density $\log_{10} \rho$ for the model \mathcal{I} at six different stages of the dynamical evolution.

Table 3: Optimum fit parameters

	$\log_{10} \mu$ (μ in $\langle M_J \rangle$)	$\log_{10} \mu$ (μ in M_\odot)	$\log_{10} \sigma$ (σ in M_\odot)	$n(\text{H}_2)$ (in cm^{-3})
$M_* = 30\%$	−0.06	−0.31	−0.53	2.3×10^5
$M_* = 60\%$	0.15	−0.31	−0.43	6.2×10^5
$M_* = 90\%$	0.31	−0.31	−0.49	1.3×10^6
IMF	—	−0.31	−0.38	—

Parameters of the optimum log-normal fits to the combined core mass distribution in Fig. 23. The lines $M_* = 30\%$, $M_* = 60\%$, and $M_* = 90\%$ denote the evolutionary stages where 30%, 60%, and 90% of the available gas mass is accreted onto protostellar cores. The entry IMF indicates the parameters of the mass function of multiple stellar systems (Kroupa et al. 1990, model MS). The second column denotes the peak location of the log-normal fit function (Eqn. 7) with respect to the average Jeans mass in the system. Column 3 and 4, show peak and width in units of solar mass for the physical scaling where core mass spectrum and IMF peak at the same position (i.e. when all entries in column 3 agree). The fifth column lists the corresponding physical average gas density in the system.

Figures:

Fig. 1.— Initial particle distribution for the nine SPH simulations with $\alpha = 0.01$ and $P(k) \propto 1/k^2$ projected into the xy -plane. The six models with 50 000 particles: a) \mathcal{A} , b) \mathcal{B} , c) \mathcal{C} , d) \mathcal{D} , e) \mathcal{E} , f) \mathcal{F} . Models with 200 000 particles: g) \mathcal{G} , h) \mathcal{H} . The high-resolution model with 500 000 particles: i) \mathcal{I} . Every figure contains 50 000 particles. In case of a larger total number, the plotted particles are selected randomly. Model \mathcal{F} (f) is generated from particles placed on a grid, which is still visible in the figure. All other models use random uniform particle distributions. The Zel’dovich shift applied to generate model \mathcal{E} is $\delta t = 1.0$, the shift for models \mathcal{H} and \mathcal{I} is $\delta t = 1.5$. Otherwise, $\delta t = 2.0$ is used. Therefore these distributions exhibit more structure and larger density contrasts. For a summary see Tab. 1.

Fig. 2.— Snapshots of the model \mathcal{A} at $t = 0.0$ (initial condition at the start of the SPH simulation), at $t = 0.2$, at $t = 0.5$, at $t = 0.7$, at $t = 1.0$, and at $t = 1.2$. During the dynamical evolution, small-scale fluctuations are damped, whereas Jeans unstable clumps start to collapse. At $t = 0.5$, the first compact cores (‘sink particles’ in terms of the SPH code) have formed in the centers of the densest clumps and have accreted $M_* = 5\%$ of the total gas mass. At $t = 0.7$ the protostellar cores altogether gained 10% of the available mass. Each of the following snapshots of the system is taken at the phase where the mass of the cluster of cores has increased further by 10% of the total mass. Gas particles are plotted as small dots and collapsed cores are denoted by thick dots. Note that the figures do not give information about the smoothing volume of individual particles. Its size is such that it contains roughly 50 neighbors.

Figure 2 — continued: Snapshots of the model \mathcal{A} at $t = 1.4$, $t = 1.6$, $t = 1.8$, $t = 2.1$, $t = 2.5$, and $t = 3.3$. The total gas mass accreted onto protostellar cores is $M_* = 40\%$, $M_* = 50\%$, $M_* = 60\%$, $M_* = 70\%$, $M_* = 80\%$, and $M_* = 90\%$, respectively.

Fig. 3.— Density distribution of the high-resolution model \mathcal{I} at four different times: Initially, at $t = 1.5$, at $t = 2.0$, and at $t = 2.8$. The total mass fraction accreted onto protostellar cores is denoted by M_* . The location of protostellar cores is denoted by black dots and the density is scaled logarithmically.

Fig. 4.— Density pdf for the high-resolution simulation \mathcal{I} at six different stages of the dynamical evolution of the system. (a) The initial state at $t = 0.0$. (b) At $t = 1.2$ when the first few cores have formed and contain about 1% of the total mass. (c) At $t = 1.5$ when protostellar cores account for $M_* = 10\%$ of the system mass. (d) At $t = 2.0$ and $M_* = 30\%$, (e) at $t = 2.8$ and $M_* = 60\%$, and finally (f) at $t = 2.9$ where $M_* = 90\%$, i.e. the cluster of cores contains almost all mass in the system. The dashed lines in some plots describe a linear fit with the slope $d \log_{10} N / d \log_{10} \rho$ indicated by the attached number.

Fig. 5.— Line centroid velocity pdf for the high-resolution simulation \mathcal{I} at four relevant stages of the dynamical evolution for the line-of-sight aligned with the x -, y -, and z -axes of the system: (a) At $t = 1.2$ when the first few cores have formed and contain about $M_* = 1\%$ of the total mass. (b) At $t = 2.0$ when is $M_* = 30\%$. (c) At $t = 2.8$ and $M_* = 60\%$, and finally (d) at $t = 2.9$ where almost all gas mass is accreted onto cores, $M_* = 90\%$. The dashed parabola in the main plots indicate the Gaussian distribution obtained from using the first two moments μ and σ from Tab. 2. For neither pdf those give a good fit. The inlay in the upper right corner of each figure indicate the total line profile (v versus $\log_{10} N$) obtained from summing over the velocity contribution of all particles in the system.

Fig. 6.— Properties of identified clumps and condensed cores in the high-resolution simulation \mathcal{I} at times $t = 0.0, 1.5, 2.0$ and 2.8 , i.e. when 0%, 10%, 30% and 60% of the total gas mass is collapsed onto protostellar cores. For each point in time the upper panel shows the distribution of gas clump masses (thin lines) and core masses (thick lines). The lower panel shows the location of each identified clump in a density–mass diagram. A detailed explanation is given in the main text.

Fig. 7.— Formation and accretion history of selected protostellar cores in the simulations (a) \mathcal{A} and (b) \mathcal{I} . The numbers reflect the order of their formation.

Fig. 8.— Final masses m of the protostellar cores i in the high-resolution model \mathcal{I} (black dots) and in model \mathcal{A} (stars) for comparison. Again the numbers reflect the order of their formation.

Fig. 9.— Initial distance distribution of matter that gets accreted onto protostellar cores. For (a) the first nine cores to form and for (b) the last nine ones, the number N of SPH particles that get accreted onto a condensed core are plotted as function of their initial distance r to the particle that is converted into the accreting core particle. The cores that form first accrete more mass than the later ones and this mass is accumulated from a smaller volume.

Fig. 10.— Mass contribution m_j of individual clumps j identified in the initial density field to the final mass of a core particle i : for (a) core $i = 1$, (b) core $i = 2$, (c) core $i = 10$, (d) core $i = 40$ and (e) core $i = 55$. The total mass of the gas clumps j is indicated by dots, their mass contribution to core i by crosses. Plot (f) gives the mass-weighted mean of the fraction of clump material $\langle f_i \rangle$ that gets accreted onto individual cores i . Cores that form early (small values of i) tend to accrete nearby clumps more completely, whereas material that builds up cores at later stages has already undergone sufficient dynamical evolution to be well mixed. The initial association with certain clumps becomes irrelevant.

Fig. 11.— a) Trajectories of cores #3, #5, #11, #31 and #46, projected into the xy -plane. b) Magnification of the unstable triple (#3,#5,#11) that forms early at the beginning. Core #5 gets expelled at $t \approx 0.8$. c) Enlarged view on the trajectories during the second major dynamical event at $t \approx 1.6$: the hardening of binary (#3,#11) in an encounter with object #46 and subsequent acceleration due to interaction with particle #31.

Fig. 12.— Typical shapes of identified clumps in the high-resolution model \mathcal{I} at time $t = 1.2$, i.e. when four collapsed cores have formed and accreted 1% of the total gas mass. This first part of the figure projects the clumps containing the four protostellar cores into the xy -, xz - and yz -plane. Density is scaled logarithmically. Two contour lines span one decade ($\log_{10} \Delta\rho = 1/2$) with the lowest contour level being $10^{1/2}$ above the mean density $\langle \rho \rangle = 1/8$. The black dots indicate the positions of the dense protostellar cores.

Figure 12 — continued: Typical shapes of identified clumps in the high-resolution model \mathcal{I} at time $t = 1.2$. This second part of the figure shows contour plots of clumps that have not yet collapsed to high enough densities to contain dense cores. Note that clumps are numbered according to their peak density. The plot is centered on the center-of-mass of each clump, as indicated by the two intersecting lines.

Fig. 13.— Radial surface density profiles for the xz -projection of clumps #4 and #12 in the sample. These clumps are selected because their projections appear relatively round and smooth (cf. with Fig. 12). Hence, the radially averaged density profile is a good approximation of the real density distribution. For comparison, the projected surface density Σ of an isothermal sphere is indicated by the dotted line. It has a 3-dimensional density profile $\rho(r) \propto (r^2 + r_c^2)^{-1}$ where $r_c = 0.005$ is the core radius (which is equal to the radius of the sink particle in model \mathcal{I}). Whereas the density profile flattens out for clump #12 which has yet to form a condensed core, the density for clump #4 increases all the way inwards to the central dense core. The steep density fall-off at $\log_{10} R \gtrsim -0.8$ is an artifact of the clump search algorithm. At these radii the clumps blend into the background gas and an artificial boundary is introduced.

Fig. 14.— Clustering properties of the protostellar cluster. The left panel plots the location of protostellar cores projected into the xy -, the xz - and yz -plane, respectively, at (a) $t = 1.0$, (b) $t = 2.0$, (c) $t = 3.0$, and (d) $t = 5.0$. The right panel shows the projected mean surface density of companions ξ for protostellar cores as function of separation r . Data are taken from model \mathcal{A} since it has been advanced furthest in time.

Fig. 15.— Distribution of semi-major axes for identified bound pairs of protostellar cores in model \mathcal{A} at times (a) $t = 1.0$, (b) $t = 2.0$, (c) $t = 3.0$, and (d) $t = 5.0$. The times are chosen in analogy to the previous figure. For cores associated with higher-order systems this gives only a rough estimate of the orbital parameters.

Fig. 16.— Time evolution of the angular momenta \vec{L} of protostellar cores. The left column plots (a) the x -component L_x , (c) the y -component L_y and (e) the z -component L_z of each condensed core in the high-resolution simulation \mathcal{I} as function of time t . The right column plots the distribution of every component at the end of the SPH simulation. For model \mathcal{I} at $t = 3.9$ (solid lines) and for comparison form for model \mathcal{A} at $t = 5.6$ (dashed lines): (b) L_x , (d) L_y and (f) L_z .

Fig. 17.— (a) Distribution of the total angular momenta $|\vec{L}|$ of protostellar cores in the simulation \mathcal{I} at $t = 2.8$ (solid lines), i.e. when 60% of the gas has been accreted, and at the final stage $t = 3.9$ (dashed lines). (b) Distribution of the specific angular momenta $|\vec{L}|/m$ at the same times. (c) Specific angular momentum $|\vec{L}|/m$ as function of the mass m of the cores (filled circles denote $t = 2.8$ and open circles the final state $t = 3.9$).

Fig. 18.— Projection of the angular momenta \vec{L} of protostellar cores in simulation \mathcal{I} into the xy -, xz - and yz -plane at $t = 1.5$ (upper panel), $t = 2.0$ (middle panel) and $t = 2.8$ (lower panel), i.e. when 10%, 30% and 60%, respectively, of the gas mass is accreted onto the cores. The length of the lines is proportional to $|\vec{L}|$; note that for better legibility the scaling factor in the bottom row is reduced by a factor of 1/3 compared to the upper two panels.

Fig. 19.— Energetic properties of the protostellar clusters that form in model \mathcal{A} (dashed lines) and model \mathcal{I} (solid lines): Time evolution of (a) the total kinetic energy, subdivided into the contribution from random motions E_{int} (thick lines) and from the center-of-mass motion E_{cm} (thin lines at the bottom of the plot), (b) the potential energy E_{pot} , (c) the virial coefficient $\eta_{\text{vir}} \equiv 2E_{\text{int}}/|E_{\text{pot}}|$, and (d) the cumulative mass M_{tot} of the cluster.

Fig. 20.— Time evolution of the total (3-dimensional) velocity dispersion σ (thick lines), of the line-of-sight velocity dispersion along the x -, y - and z -axis (thin lines) and of the center-of-mass velocity (thin lines at low velocities) of the protostellar cluster that forms during the dynamical evolution of the standard model \mathcal{A} (dashed curves) and the high-resolution model \mathcal{I} (solid curves).

Fig. 21.— Mass distribution of protostellar cores in the high-resolution model \mathcal{I} at different stages of the dynamical evolution. In the upper right corner of each plot, the time t and the fraction of the total gas mass converted into protostellar cores M_* is indicated. Analog to Fig. 6, the vertical line indicates the mass resolution limit of the simulation.

Fig. 22.— Distribution of protostellar core masses for all models described in this chapter (Tab. 1) at the stage when roughly 60% of the gas mass is accumulated in condensed cores: (a) corresponds to model \mathcal{A} , (b) to model \mathcal{B} , and so forth.

Fig. 23.— Combined distribution of core masses in all simulations with $\alpha = 0.01$ and $P(k) \propto 1/k^2$ at times when 30%, 60% and 90% of the total gas mass has been converted into protostellar cores. The open circles denote the best fit Gaussian (see Tab. 3) and the dashed curve in each plot specifies the IMF for multiple stellar systems (Kroupa et al. 1990). The system is scaled such that the maxima of both distributions agree — recall that the core mass distribution peaks roughly at the average Jeans mass of the system. For comparison the dotted curve shows the original Miller & Scalo (1979) mass function (for constant star formation over 12×10^9 years), shifted to the same peak mass.

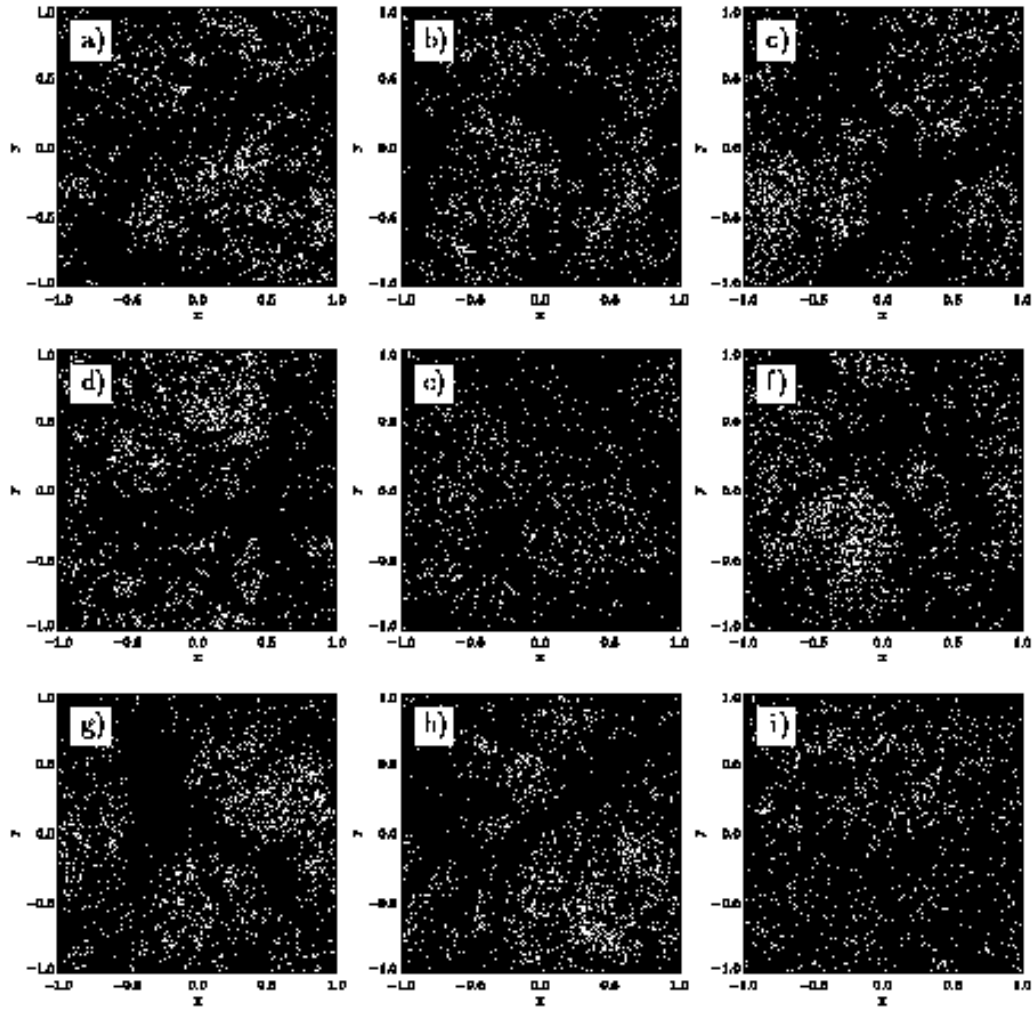
Fig. 24.— Illustration of the clump finding algorithm in a 1-dimensional sample case: At the highest density level one clump is identified and all particles at this level get assigned to it. At the third level an additional clump is detected. At the sixth highest level, a third new clump is identified. Clumps #1 and #2 now have overlapping contour lines and are separated as described above. This is indicated by an arrow. At level eight the last clump is detected and separated from the other at the lowest level (again indicated by arrows).

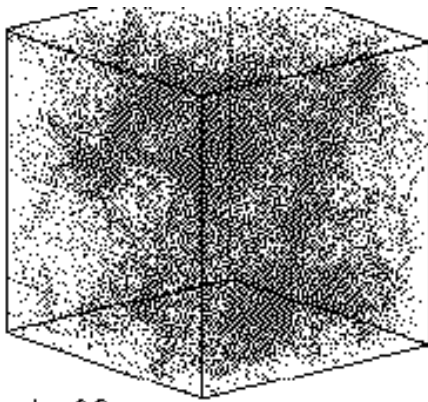
Fig. 25.— Projections of the particle distribution generated by the Zel’dovich method from a power spectrum $P(k) \propto k^{-2}$. (a) Homogeneous starting distribution. The distribution after applying the Zel’dovich method with (b) $\delta t = 1/2$, (c) $\delta t = 1$, (d) $\delta t = 2$, (e) $\delta t = 3$, (f) $\delta t = 5$, (g) $\delta t = 10$, and (h) $\delta t = 30$. (i) The dependence of the average and maximum particle density on the time shift δt is plotted in open and filled circles, respectively. The dashed line denotes the average density of the homogeneous cube.

Fig. 26.— (a) 2-point correlation function $\xi(r)$ and (b) power spectrum $P(k)$ for different shift intervals δt . To compute the functions, the cube has been subdivided into $(128)^3$ cells. The random homogeneous starting distribution is plotted with dotted lines. The statistical errors for different distances r and wave numbers k apply to all fields equally.

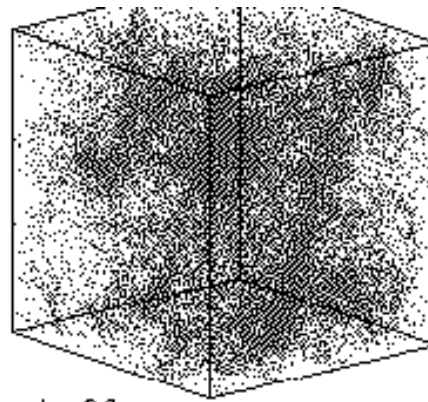
Fig. 27.— Snapshots of the evolution of a system generated by the Zel’dovich method from a power spectrum $P(k) \propto k^{-2}$ and shift interval $\delta t = 2$. After applying the Zel’dovich shift, the subsequent evolution is calculated using SPH. The figures show projections of the 3-dimensional distribution into the xy -plane in intervals of $\Delta t = 0.3$: (a) initially at $t = 0.0$, (b) at $t = 0.3$, (c) at $t = 0.6$, (d) at $t = 0.9$, (e) at $t = 1.2$, and (f) at $t = 1.5$. Time is measured from the begin of the SPH simulation.

Fig. 28.— Analogous to Fig. 27, but describing a system that is entirely evolved in time using SPH. No Zel’dovich shift is applied. The system is projected into the xy -plane at (a) $t = 0.0$, showing the homogeneous starting condition, at (b) $t = 1.0$, (c) $t = 1.7$, (d) $t = 2.0$, (e) $t = 2.3$, (f) at $t = 2.6$, (g) at $t = 2.9$, (h) at $t = 3.2$, and (i) at $t = 3.5$. Again, time is measured from the begin of the SPH simulation.

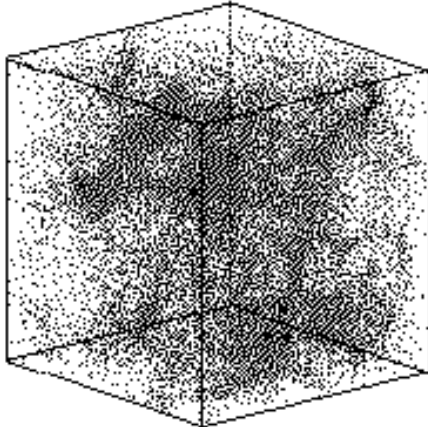




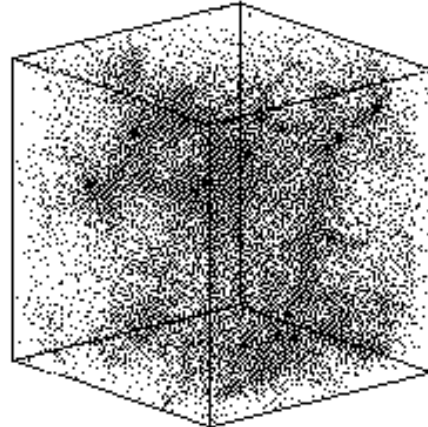
$t = 0.0$
 $M_{\perp} = 0\%$



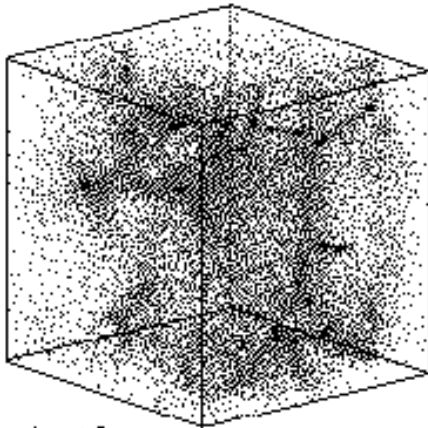
$t = 0.2$
 $M_{\perp} = 0\%$



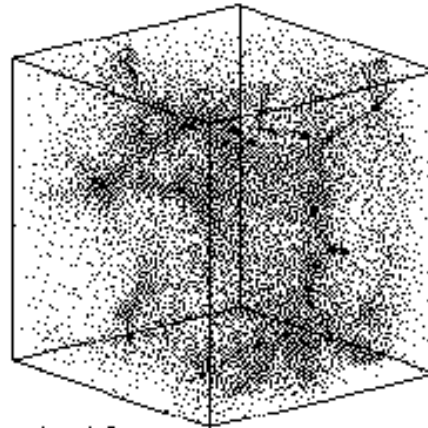
$t = 0.5$
 $M_{\perp} = 5\%$



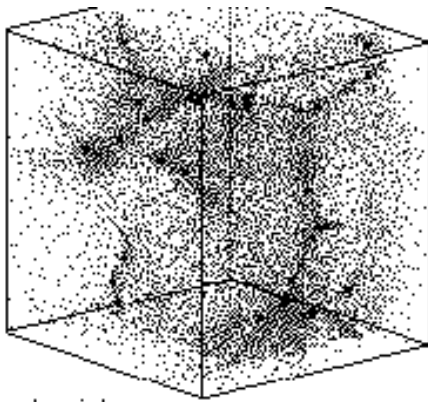
$t = 0.7$
 $M_{\perp} = 10\%$



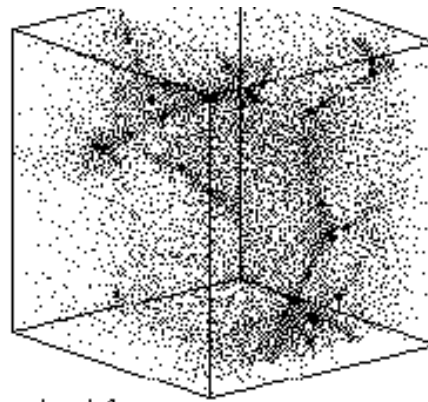
$t = 1.0$
 $M_{\perp} = 20\%$



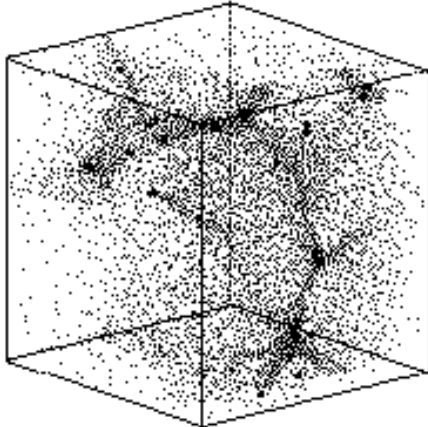
$t = 1.2$
 $M_{\perp} = 30\%$



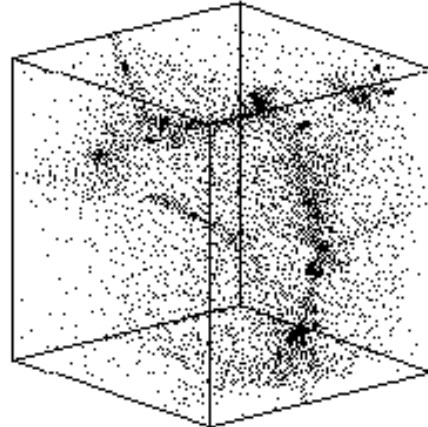
$t = 1.4$
 $M = 40\%$



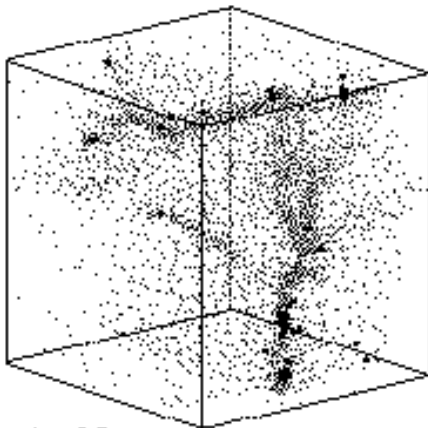
$t = 1.6$
 $M = 50\%$



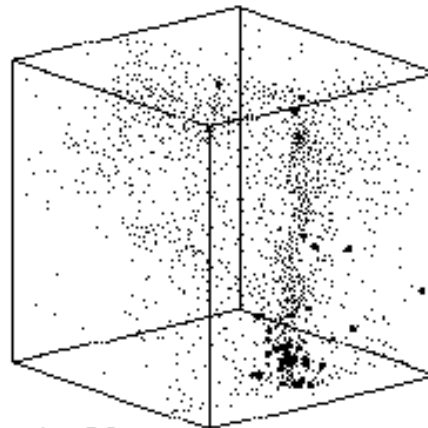
$t = 1.8$
 $M = 60\%$



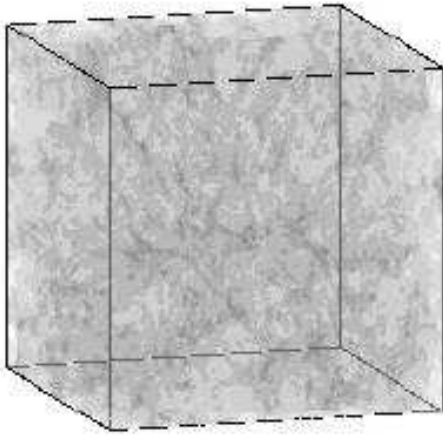
$t = 2.1$
 $M = 70\%$



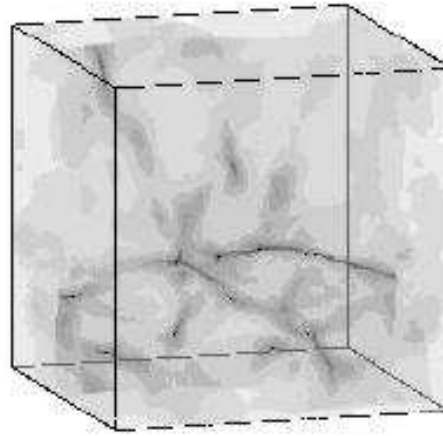
$t = 2.5$
 $M = 80\%$



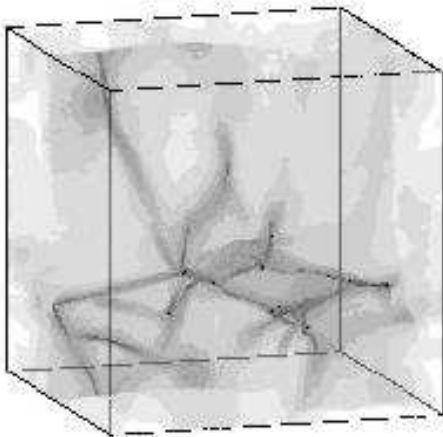
$t = 3.3$
 $M = 90\%$



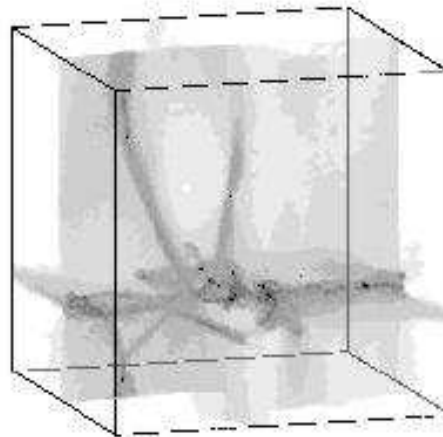
$l = 0.0$
 $M_c = 0\%$



$l = 1.5$
 $M_c = 10\%$



$l = 2.0$
 $M_c = 30\%$



$l = 2.8$
 $M_c = 60\%$

